Journal of Ultrasound (2020) 23:227–257
https://doi.org/10.1007/s40477-020-00477-4

PICTORIAL ESSAY

Ultrasound and bone: a pictorial review

Stefano Bianchi[1]

Received: 25 April 2020 / Accepted: 6 May 2020 / Published online: 17 May 2020

Abstract
The assessment of bone mainly relies on standard radiographs, CT, MRI, and bone scintigraphy depending on the anatomic region complexity and clinical scenario. Ultrasound (US), due to different acoustic impedance between soft tissues and the bone cortex, only allows the evaluation of the bone surfaces. Nevertheless, US can be useful in the evaluation of several bone disorders affecting the limbs as a result of its tomographic capabilities and high definition. This pictorial review article summarises our clinical experience in adults and reviews the literature on US bone examination. We first present the US appearance of normal bone and the main congenital anatomic variations, after which we illustrate the US findings of a variety of bone disorders. Although US has limits in bone assessment, its analysis must be a part of every musculoskeletal US examination.

Keywords Bone · Ultrasound · Congenital conditions · Trauma · Infections · Tumours

Normal US anatomy

The normal bone appears as a hyperechoic continuous line related to the interface between the outer cortex and the adjacent tissues on US (Fig. 1) [1–6]. The periosteum covers the outer surface of bone, with the exception of the site of tendons, fasciae, and ligament insertion. It allows vascularisation to the bone, has osteogenic properties, and also has a mechanical role, since it receives fibres from tendons [4, 7]. The normal periosteum in adults can be barely visualised as a thin hypoechoic band, while the thicker periosteum in children is easily detected at US [4]. The normal hyperechoic bone surface can present irregularities. Localised discontinuities are found where nutrient arteries enter the bone. In children, the cartilage growth plates appear as a wider interruption of the cortex localised between the metaphysis and epiphysis. Non-fusions of accessory ossification centres appear as osseous fragments with a rounded border, separated from the adjacent main bone. Prominences of the surface of the cortex are found at the insertion of tendons and ligaments.

✉ Stefano Bianchi
stefanobianchi@bluewin.ch

[1] CIM SA Cabinet Imagerie Médicale, 40a route de Malagnou, 1208 Geneva, Switzerland

Congenital conditions

Non-fusion of the ossification centres

Non-fusion of the ossification centres of bones is a common anatomic variation [8, 9]. The unfused bone centre (UBC) is linked to the adjacent bone by a fibrous synchondrosis and appears at US as an ossicle with roughly rounded borders. Most UBCs are incidental and asymptomatic findings [10]. Nevertheless, post-traumatic separations or fractures through the synchondrosis can lead to UBC instability, inflammation, and pain [10]. The main US differential diagnosis of symptomatic UBC is fractures or soft-tissue calcifications. Standard radiographs and CT detect most UBC, but cannot appreciate the presence of local inflammation. MRI and bone scan allow an optimal assessment of local inflammation as a bone marrow and soft-tissue oedema at MRI and increased local activity at bone scan. US detects UBC as hyperechoic well-corticated fragments with posterior shadowing. The adjacent soft tissues are normal, without oedema or hypervascularisation at colour Doppler. In symptomatic patients, dynamic US can show instability of the UBC during the movements of adjacent joints or when pressure is applied through the transducer. Hyperaemia at colour Doppler reflects local inflammation. Differentiation of the UBC from fractures relies mainly on clinical data. In fractures, US shows sharp borders of fragments, while UBCs have

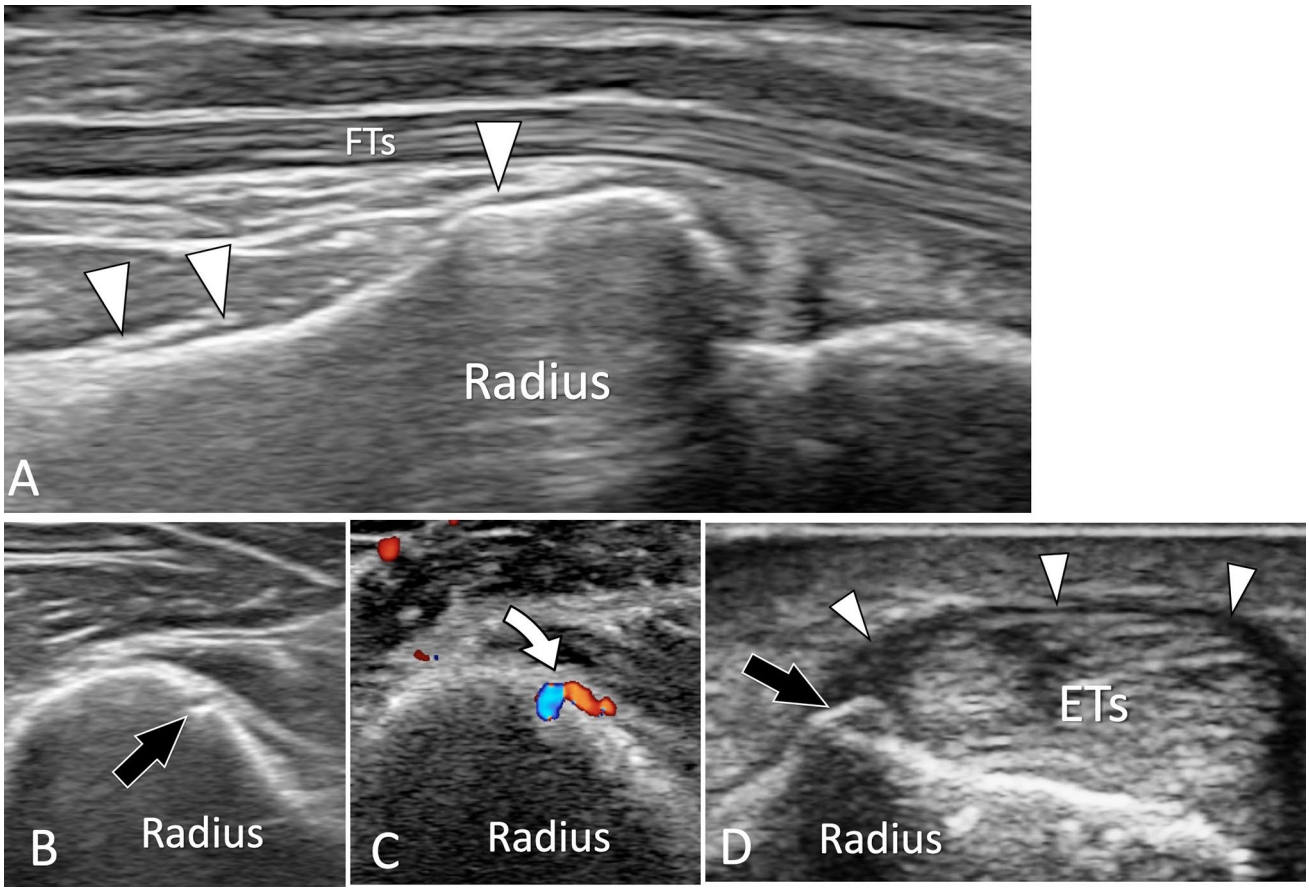

Fig. 1 US of normal adult bone. **a** Longitudinal sonogram obtained aver the palmar aspect of the distal radius. The normal periosteum of the radius (white arrowheads) appears as a thin hypoechoic band located on the bone palmar cortex. **b**, **c** Axial conventional (**b**) and colour Doppler (**c**) sonograms obtained at the middle of the radius. In **b** note, a focal break in the cortex which corresponds in **c** to the location where the nutrient artery (curved arrow) enters the bone. **d** Axial US image obtained over the radial aspect of the distal radius. US shows a small bone ridge at the insertion of the retinaculum (white arrowheads) of the first compartment of the extensor tendons (ETs)

well-defined rounded borders. The distinction from dense soft-tissue calcifications can be difficult at US and sometimes requires correlation with radiographs. Most symptomatic UBCs are treated by rest and medications, while a few needs surgical resection [11].

Os acromiale

Os acromiale results for failure of fusion of the anterior ossification centre of the acromion [12]. When unstable, os acromiale can be associated with rotator cuff pathology [13]. US shows a local interruption of the superior cortex of the acromion associated with some local bone spurs (Fig. 2). The inexperienced sonologist can misinterpret this as degenerative changes of the acromion-clavicular (AC) joint. Once detected, the ossicle must be carefully evaluated for size in the greater diameter and local hyperaemia at colour Doppler. Sometimes, real-time examination during local compression through the transducer can detect instability of the unfused centre. Instability, when symptomatic and associated to rotator cuff pathology, is frequently treated by surgical resection. If indicated clinically, US can accurately guide a local steroids/lidocaine injection as a diagnostic and therapeutic test. There is still lack of consensus in the preferred treatment of painful os acromiale [14].

Patella bipartita

The most frequent type of patella bipartita is type II, which affects the superolateral quadrant [11, 15]. US habitually detects patella bipartita in symptomatic patients examined for a potential tendon lesion. US appearance of patella bipartita is similar to that of os acromiale. In seven patients with patella bipartita, Blankstein described an irregularity of the bony contour associated with a cleft between patella and the superolateral UBC [16]. Local hyperaemia at the interface reflects inflammation due to instability of the UBC (Fig. 3).

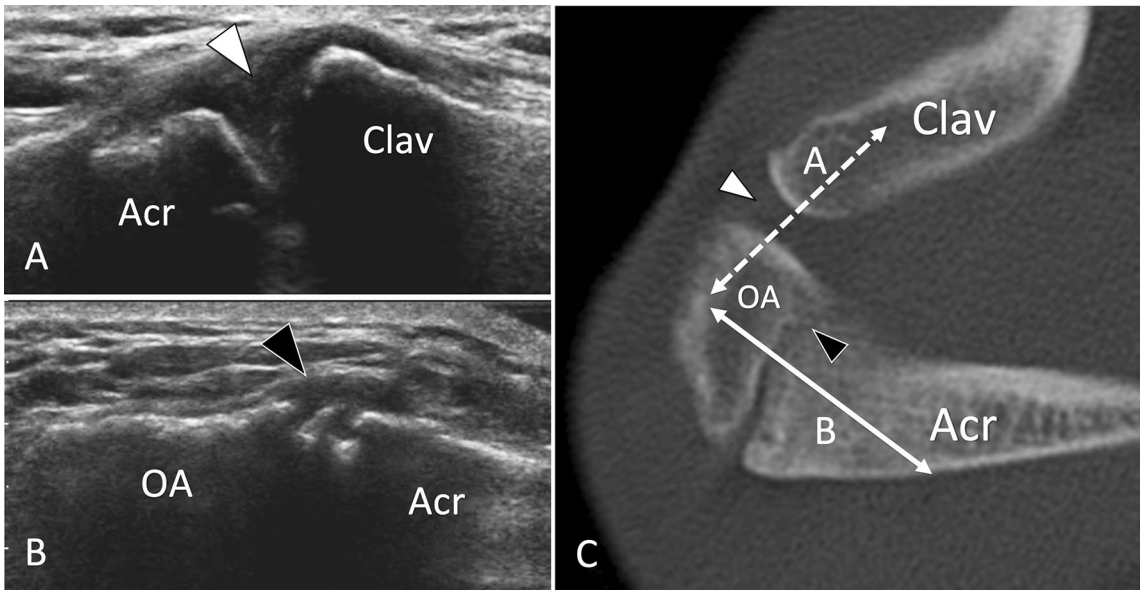

Fig. 2 Non-fusion of ossification centres. Asymptomatic os acromiale. US (**a**, **b**) with axial CT (**c**) correlation in a patient with os acromiale. Sonogram **a** obtained over the acromioclavicular joint (line A in C) shows the normal joint (white arrowhead). Note smooth borders of bone ends. **b** US image obtained over the Os acromiale (OA) (line B in C) exhibits a focal interruption (black arrowhead) of the hyperechoic line corresponding to the bone surface due to non-fusion of the os acromiale. In **b**, **c,** note the rough borders of the non-fusion

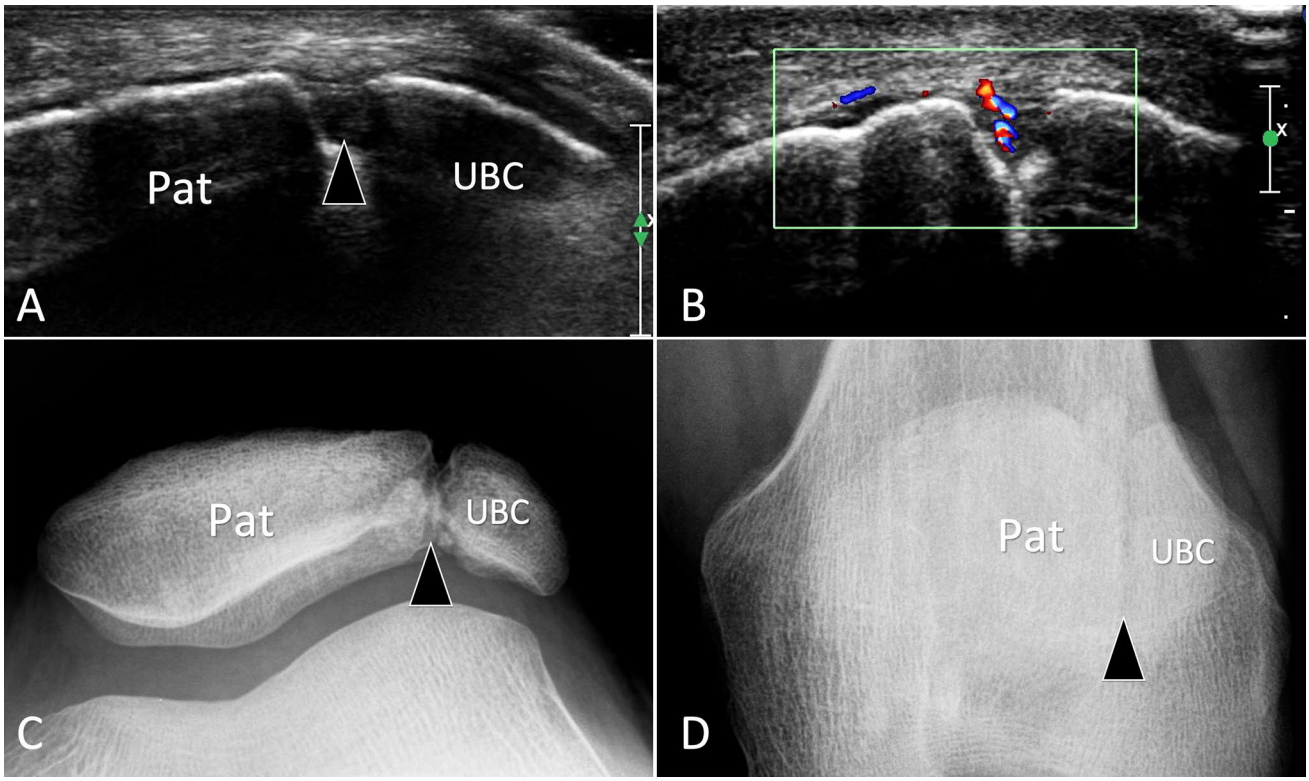

Fig. 3 Non-fusion of ossification centres. Symptomatic patella bipartita. **a**, **b** Axial grey scale (**a**) and colour Doppler **b** sonograms with **c**, **d** sunrise (**c**) and A–P (**d**) standard radiographs. In **a** obtained at the anterior aspect of the patella (Pat), note the break (arrowhead) of the bone cortex related to synchondrosis between the patella and the unfused bone centre (UBC). **b** Local hyperaemia due to instability of the UBC. **c**, **d** Standard radiographs confirms US appearance

A US-guided local lidocaine injection can confirm non-fusion as the origin of pain.

Others

Others examples of non-fusion of ossification centres suitable of US assessment include the accessory tarsal navicular [17] (Fig. 4) and os hamuli proprium [18] (Fig. 5).

Bone coalition

Bone coalitions are developmental conditions that occur when two adjacent bones are connected with a bridge that can be fibrous, cartilaginous or osseous. Most coalitions affect the talocalcaneal, calcaneo-navicular and talonavicular joints. Upper extremity coalitions are uncommon and mostly observed at the lunotriquetral and radioulnar joints. US detects talocalcaneal bone coalition as a continuous hyperechoic line joining the two bones [19] (Fig. 6). In the more common fibrous coalition, US shows local beak-like bony excrescences that mimic degenerative changes [19]. The advantage of US in coalition detection relies on its tomographic nature that allow their recognition also in patients with negative or doubtful radiographs. In addition, US, as well as MRI, can assess the pathological changes of tendons and nerves due to impingement with the aggressive borders of the coalition [19, 20]. CT and MRI are required in pre-surgical planning. Bone coalitions are differentiated by bone ankylosis following longstanding rheumatoid arthritis by correlating the US appearance with clinical data.

Hyperplasia

Peroneal tubercle

The peroneal tubercle (PT) is a small bone protuberance found at the lateral aspect of the calcaneum that acts as a pulley for the peroneal longus tendon [21]. An anatomic

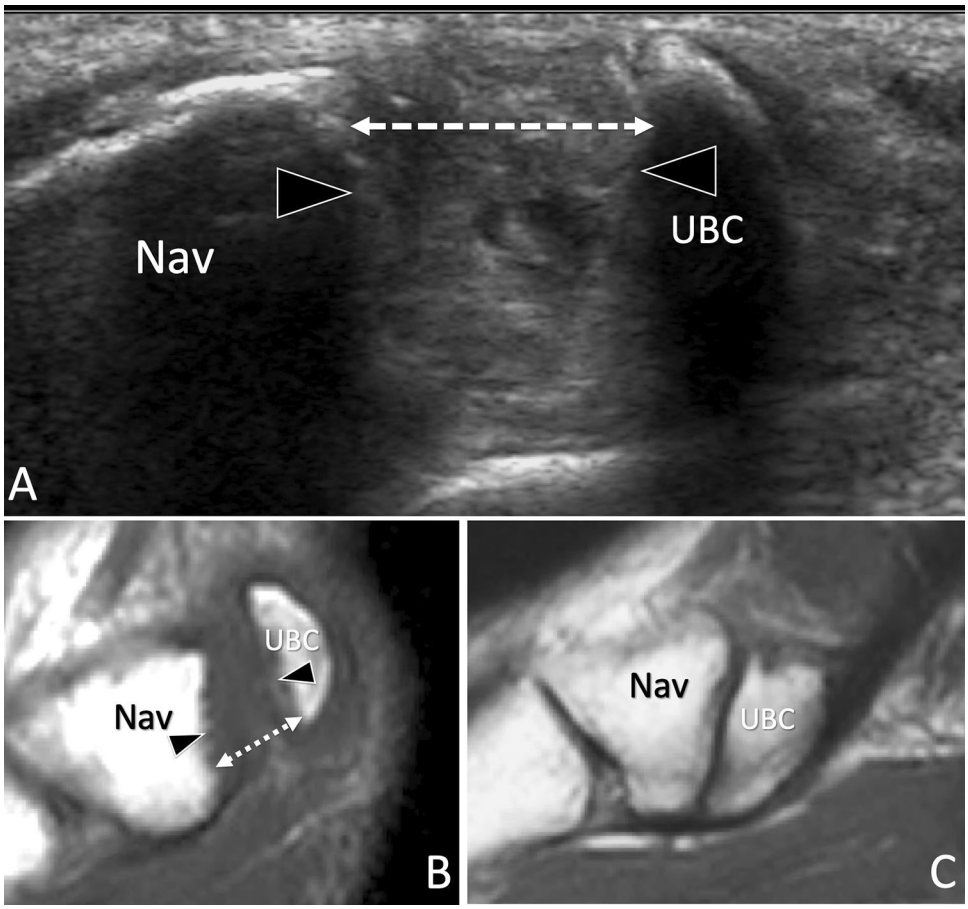

Fig. 4 Non-fusion of ossification centres. Symptomatic avulsed accessory navicular. **a** Axial oblique grey scale and **b**, **c** sagittal T1-weighted MR images obtained (**b**) at the same level and then (**a**) at the contralateral ankle (**c**). In **a** obtained at the medial aspect of the navicular bone (Nav), note the break (arrowheads) of the bone cortex related to avulsion of the unfused bone centre (UBC). The centre is retracted posteriorly (dotted double arrow) due to traction from the tibialis posterior tendon. In **b,** MR confirms the retraction of the UBC. Note normal appearance of the navicular in **c**

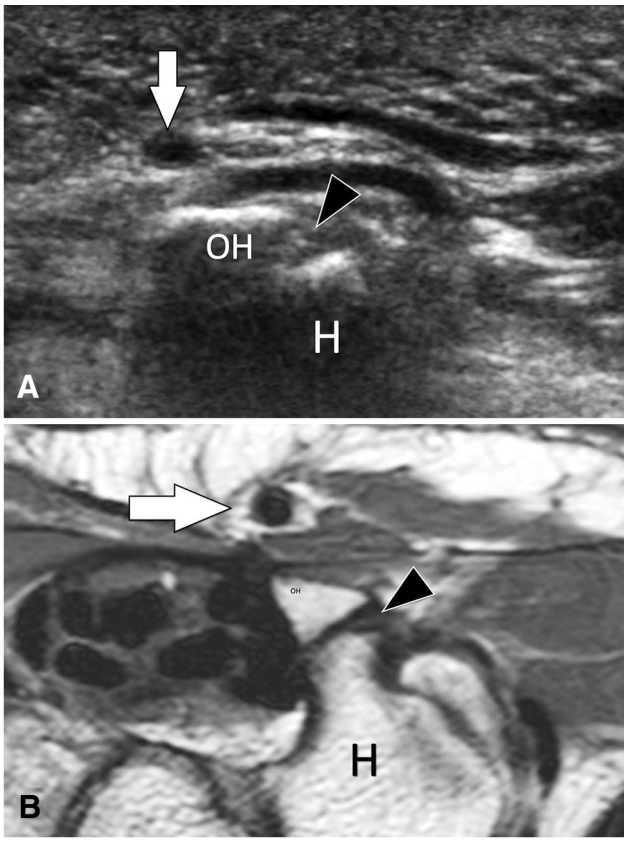

Fig. 5 Non-fusion of ossification centres. Asymptomatic os hamuli proprium. US (**a**) with axial T1-weighted MR image (**b**) correlation in a patient with os hamuli proprium. Sonogram **a** obtained over the palmar aspect of the wrist shows a focal interruption (black arrowhead) of the hyperechoic line of the ulnar aspect of the hamatum (H) corresponding to non-fusion of the ossification centre. In B, the MR image confirms the US findings. White arrows = ulnar artery

study on 114 calcaneal specimens revealed a PT in 90.4% of specimens [21]. In an MRI prospective study of 65 healthy volunteers, Saupe et al. found the PT in 55% of ankles [22]. Hyperplasia of the PT can be associated with peroneal tendons disorders [23], chiefly peroneus longus stenosing tenosynovitis and ruptures (Fig. 7). Saupe evaluated that the cut-off to diagnose a hypertrophied PT was 5 mm [22]. The PT can be easily detected at US because of its superficial position. Measurement of its height requires accurate scanning in the coronal oblique plane. In addition to PT evaluation, US permits a detailed assessment of both peroneal tendons and of their common synovial sheath [23, 24]. When a surgical resection of the enlarged PT is necessary, CT is usually performed.

Hypoplasia/aplasia

Hook of the hamate

The hamate bone is located at the distal-ulnar wrist. It is made by a large body and a protuberance pointing anteriorly, the hook of the hamate (HH). Variations in size of the HH are more frequent than previously thought [18]. In an anatomic study on 2000 hamates, Huang evaluated the height of the HH to 9.8 ± 1.4 mm. In 3.1%, the HH showed a statistical decrease in size defined as hypoplasia (height less than 7 mm) or aplasia (height less than 4 mm) [25]. Chow et al. studied hyo/aplasia of the HH using carpal tunnel view radiographs and found a significantly higher incidence in patients affected by CTS [26]. US visualises the HH in axial sonograms or when a specialised view is used [27] and can detect hypo/aplasia (Fig. 8). HH hypoaplasia predisposes to instability of the small finger flexor tendons in patients with the previous carpal tunnel surgery [28]. Dynamic US can easily detect intermittent tendons dislocation over the HH during finger's flexion/extension.

Glenoid hypoplasia

Glenoid hypoplasia is a rare developmental condition of unknown origin in which the lower part of the glenoid cavity is hypoplastic [29]. The condition is usually diagnosed at plain radiography in young patients presenting pain/limitation of motion due to secondary degenerative changes or instability of the shoulder. Although glenoid hypoplasia is mostly detected by X-rays, it can be suspected at US performed as a first examination of a painful shoulder syndrome in young subjects (Fig. 9). Once suspected at US, the diagnosis must be confirmed by standard radiographs.

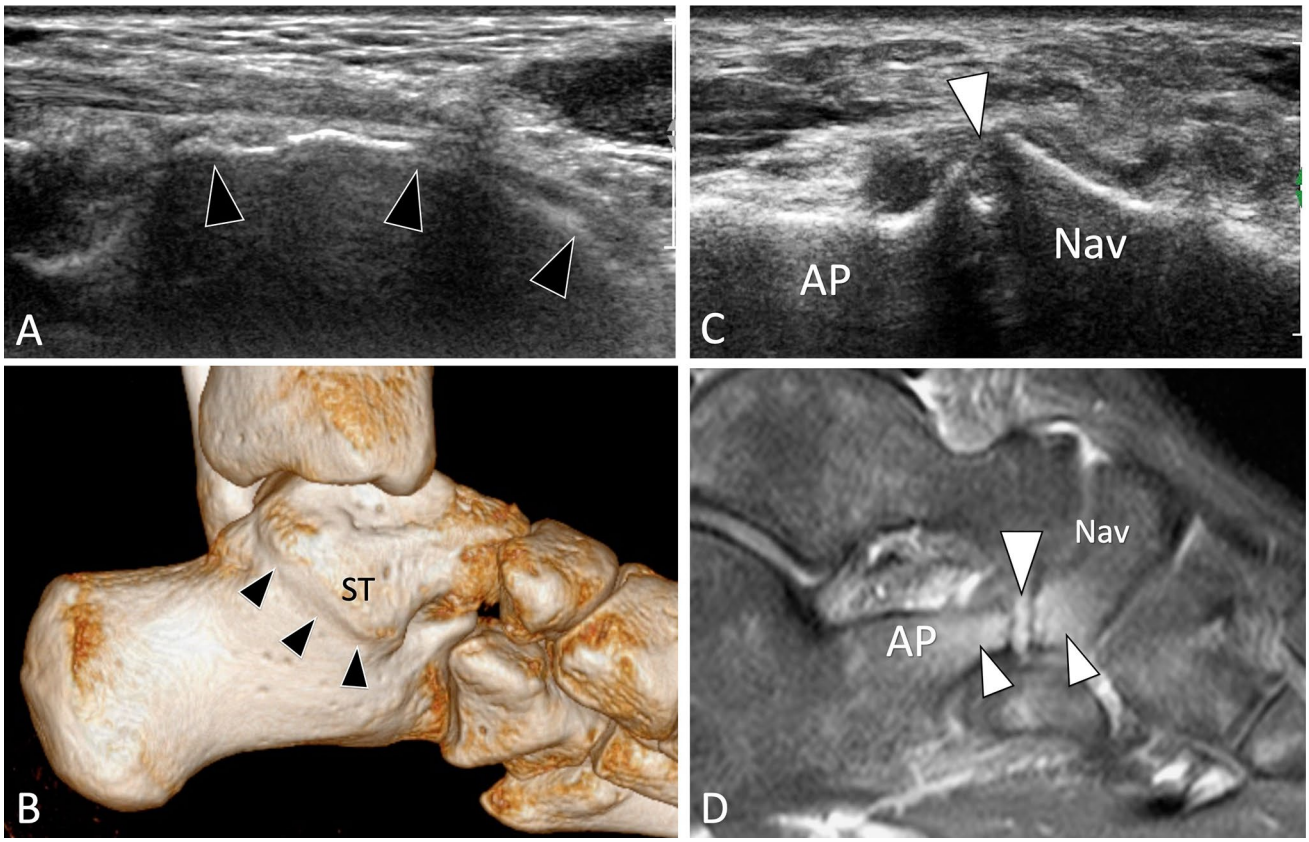

Fig. 6 Bone coalition. Symptomatic avulsed accessory navicular. **a**, **b** Coronal oblique US (**a**) and 3D CT reformatted image (**b**) in a patient with talocalcaneal osseous collation. **c**, **d** Axial oblique sonogram (**c**) and PD fat Sat sagittal MR image (**d**) in a patient with calcaneonavicular fibrous coalition. **a** US shows a continuous hyperechoic line (black arrowheads) joining the two bones. **b** CT confirms the complete bone coalition (black arrowheads). *ST* substentaculum tali. **c** The fibrous coalition appears as a beak-like pseudo-joint with irregular borders (white arrowhead). In **d,** MR confirms the coalition (white arrowhead) and images oedema of the bone marrow (small white arrowheads) due to inflammation related to local impingement

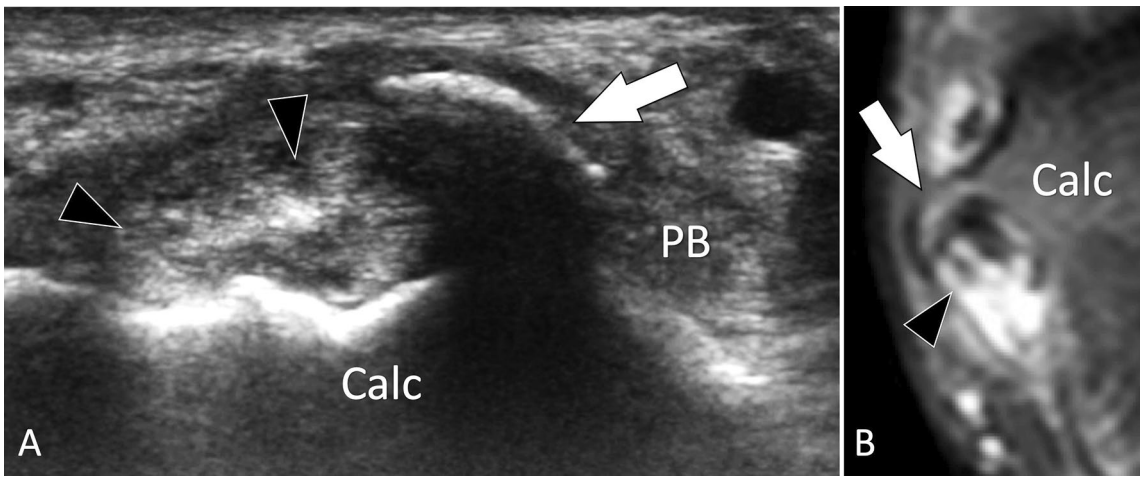

Fig. 7 Bone hyperplasia. Symptomatic hyperplastic peroneal tubercle. **a**, **b** Coronal oblique US (**a**) and PD fat Sat coronal MR image **b** in a patient with symptomatic hyperplastic peroneal tubercle. **a** US shows a hyperplastic "beak-like" peroneal tubercle (arrow). The tubercle impinges on the peroneus longus tendon that appears irregular (arrowheads). The peroneus brevis tendon (PB) is normal. **b** MRI confirms the US appearance. Note oedema of the tubercle and longitudinal split of the peroneus longus tendon (arrowheads) associated with tenosynovitis

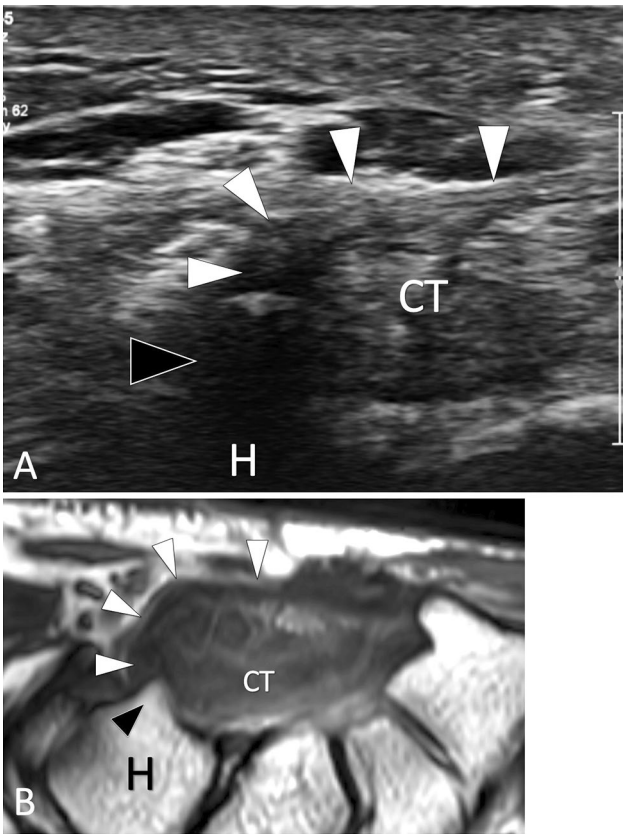

Fig. 8 Bone hypoplasia. Hypoplasia of the hook. **a** Axial US and **b** PD axial MR image in a patient with hypoplasia of the hook of the hamate. US shows a small (black arrowhead) hook of the hamate bone (H). Note the transverse carpal ligament (white arrowheads) inserting on the tip of the hook. *CT* carpal tunnel. **b** MRI confirms the US appearance

Sternal foramen

A sternal foramen is an asymptomatic full-thickness focal defect due to an incomplete fusion and ossification of the cartilaginous sternum (Fig. 10). It occurs in 2.5–13.8% of the population [30]. Awareness of a sternal foramen is important, because it must not be confused with an osteolytic lesions at imaging. Most importantly, blinded sternal punctures in patients with a sternal foramen can be complicated by cardiac tamponade [31]. Babinski et al. suggested that a previous CT must be performed before sternal acupuncture to avoid fatal complications [32]. US appearance of sternal foramen has been previously described [33]. The foramen appears as a well-defined discontinuity located in the sternum and acts as "a window" allowing visualisation of the underlying heart. The regular continuous surface of the foramen and the normal appearance of the local soft tissues indicate an anatomic variant more than a lytic bone lesion.

Traumatic disorders

Occult acute fractures

General considerations

The first-line imaging technique in the detection and assessment of acute fractures (AF) is standard radiographs. US, performed to evaluate post-traumatic soft-tissue changes, has shown to be able to identify occult fractures undetected by the previous X-ray [27, 34–36]. The US findings must be always correlated to clinical data (presence and type of trauma) and physical examination (local swelling and pain at palpation) [37]. The possibility to detect an AF by US must be known by the sonologists who must suggest further investigations, if clinically necessary.

The US hallmark of an AF is a localised interruption of the hyperechoic line corresponding to the outer bone cortex [36, 38]. Associated findings are abnormalities of the periosteum (sub periosteal hematoma), adjacent soft tissues (local haematoma, oedema, and bursitis) and joints (articular effusion in intra-articular fractures and intra-articular loose bodies). Other bony irregularities can mimic a fracture at US [36]. They include vascular channels and UBC. Vascular channels can be easily differentiated, since they are well localised and non-associated with soft-tissue oedema. Colour Doppler shows the nutrient vessel entering the cortex. The US differential diagnosis with UBC has been previously discussed. It must be underlined that non-fusions can

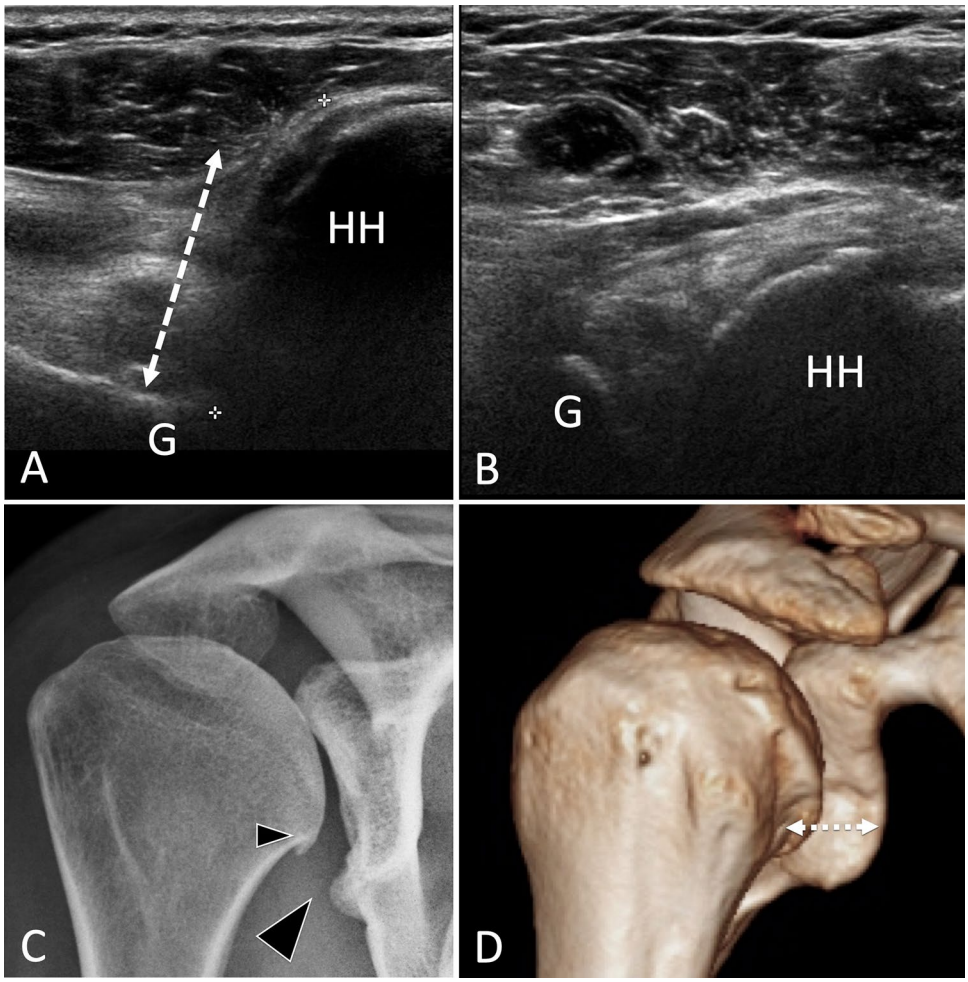

Fig. 9 Bone hypoplasia. Glenoid hypoplasia. **a**, **b** Posterior (**a**) and anterior (**b**) axial US of the gleno-humeral joint. **c** A-P standard radiograph and **d** 3D reconstructed CT of the shoulder. US shows a posterior displacement (double dotted arrow) of the humeral head (HH) with respect to the glenoid (G). The radiograph images hypoplasia of the inferior glenoid and a small osteophyte of the humeral head. In **d,** the posterior instability of the humerus is evident

be painful [11, 39], after trauma and can show local inflammatory changes at US.

Upper limb

Clavicle and scapula US can detect fractures of the clavicle and scapula [40]. The coracoid process can barely be assessed by standard radiographs because of its orientation and superimposition with the adjacent bone structures. In a retrospective study of US rotator cuff examinations in post-traumatic patients, Botchu et al. found seven coracoid fractures that were not detected by standard radiographs [41]. Fractures were imaged as a break in the upper cortex of the coracoid, associated with a variable degree of displacement and pain at local pressure under US guidance. The authors described a specialised view the "apical sonographic view", obtained tilting the transducer cranially when examining the anterior coracoid, which enabled the optimal detection of the fracture [41]. This view does not require changes in the shoulder position and, in our opinion, must be performed in every patient with post-traumatic anterior shoulder pain [42].

Humerus Greater tuberosity fractures, when minimally displaced, can be missed at radiographs [34, 43]. In a retrospective study of 31 patients with post-traumatic shoulders

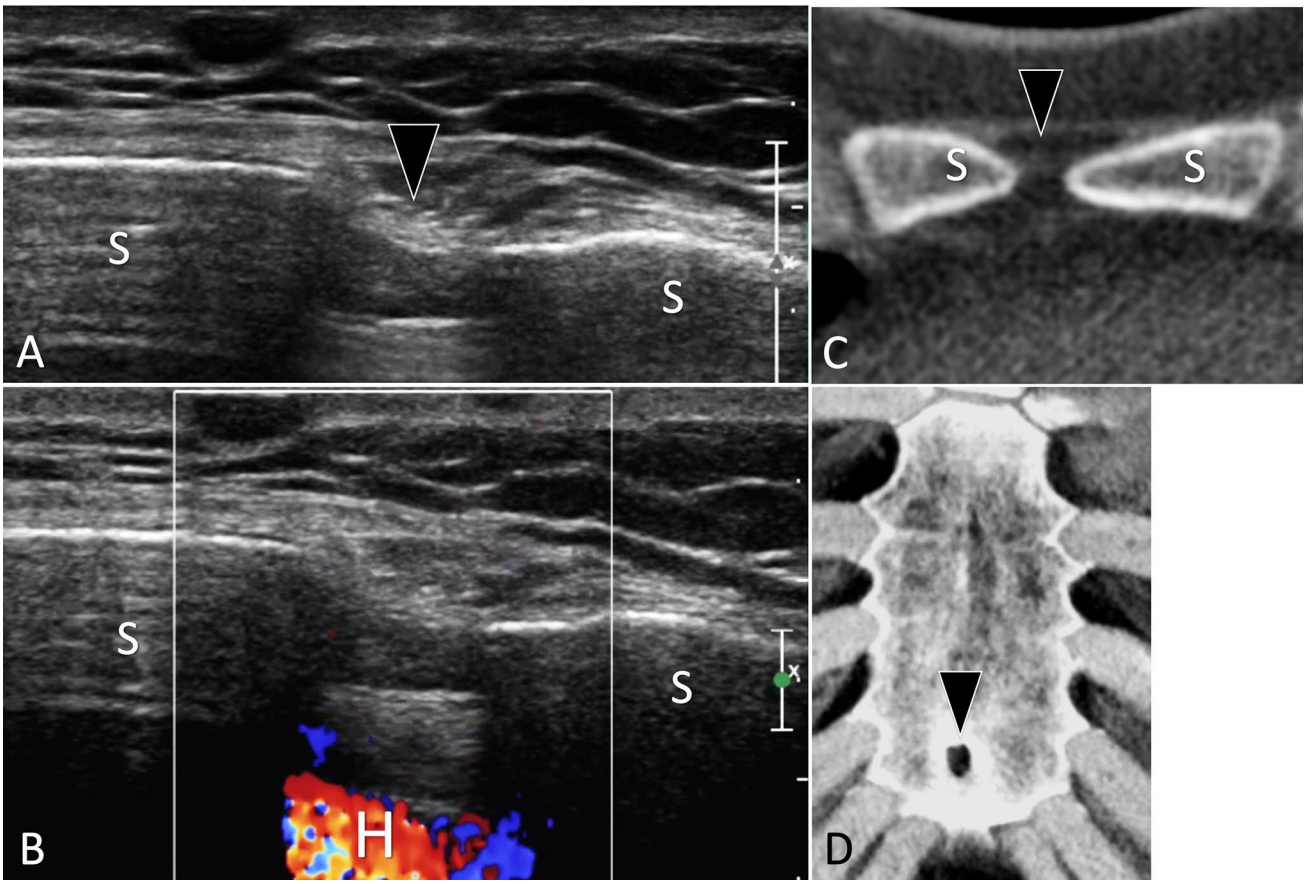

Fig. 10 Bone hypoplasia. Sternal foramen. **a**, **b** Axial grey scale (**a**) and colour Doppler (**b**) US of the anterior cortex of the sternum. **c**, **d** Axial native (**c**) and **d** 3D reconstructed CT of the sternum. In **a.** US shows a sternal foramen as a focal discontinuity (black arrowhead) of the anterior cortex of the sternum (S). Note the regular cortex surrounding the foramen, absence of periosteal reaction, or soft-tissue masses. In **b,** note visualisation of the heart (H) due to a full-thickness interruption of the sternum. **c**, **d** CT confirms the diagnosis of a sternal foramen

and US signs of greater tuberosity fracture, radiographs confirmed the fracture in 24 patients. In 10/24 patients, the fracture was missed at the initial radiographs [43]. Patients typically have a history of a fall and present for US evaluation after 1–2 weeks because of persistent pain, to rule out a rotator cuff tendon tear. Fractures appear on US as subtle irregularities of the superior aspect of the greater tuberosity (Fig. 11). Correlation with clinical findings and pain at US-guided palpation help to establish the diagnosis.

Ribs Rib fractures are very common and mostly diagnosed by X-ray. Griffith et al. showed that US is more effective (78% vs. 12%), than the conventional radiographs in revealing ribs fractures [44]. US examination is prompt and easy to perform since focused on the painful area (Fig. 12) [45]. Pain at US-guided palpation confirms the diagnosis [46]. In anterior post-traumatic chest pain, when the ribs are normal, a careful examination of the rib cartilages must be performed. US can detect cartilage fractures and assess associ-

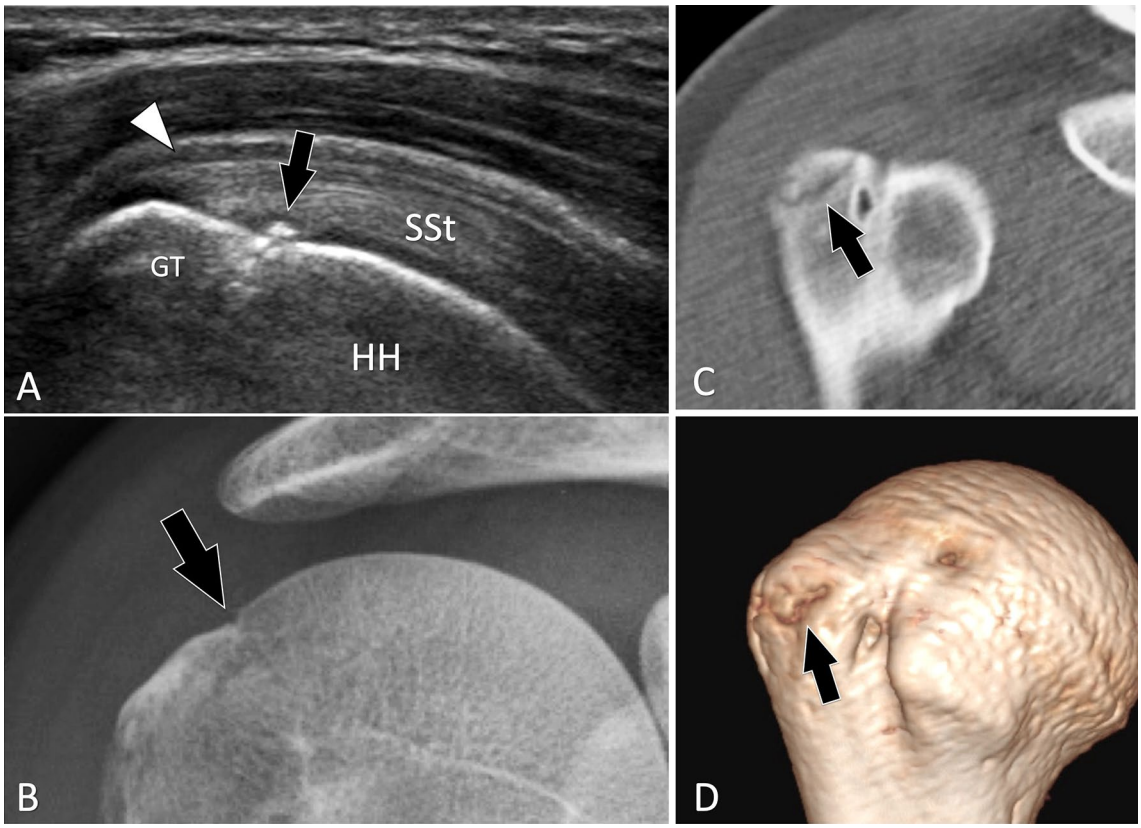

Fig. 11 Occult acute fractures. Greater tuberosity fracture. **a** Coronal oblique US obtained over the supraspinatus tendon (SSt). **b** A-P standard radiograph and **c**, **d** 2D (**c**) and 3D (**d**) reconstructed CT of the shoulder. In **a**, US shows a non-displaced fracture of the greater tuberosity (GT) of the humeral head (HH). Associated thickening of the wall of the subacromial bursa is present (white arrowhead). Standard radiographs were interpreted as normal. A second lecture made after US showed a possible "in situ" fracture (arrow). CT confirmed the US findings

ated displacement [47, 48]. In addition, US can also detect small associated pleural effusions.

Sternum Compared to standard radiographs (70.8% and 75.0%), US has a higher sensitivity and specificity (100% and 100%) for the detection of sternal fractures [49]. Fractures are better detected on sagittal sonograms as a step in the anterior cortex [33]. Independent movements of the two parts of the sternal fracture with respiration indicate simultaneous fracture of the anterior and posterior cortex. US can easily differentiate a sternal fracture from a sternal foramen.

Elbow Ultrasound imaging proved to be an effective method for the diagnosis of occult fractures of the radial head or neck when the initial radiograms showed only intra-articular effusion [50]. US confirms presence of joint effusion and can detect a focal interruption of the cortex, especially of the radial head. Axial images obtained over the head during gentle prono-supination of the forearm are useful in this field.

Carpal bones Carpal bone fractures are frequent in routine practice. Most affect the scaphoid but every bone can be

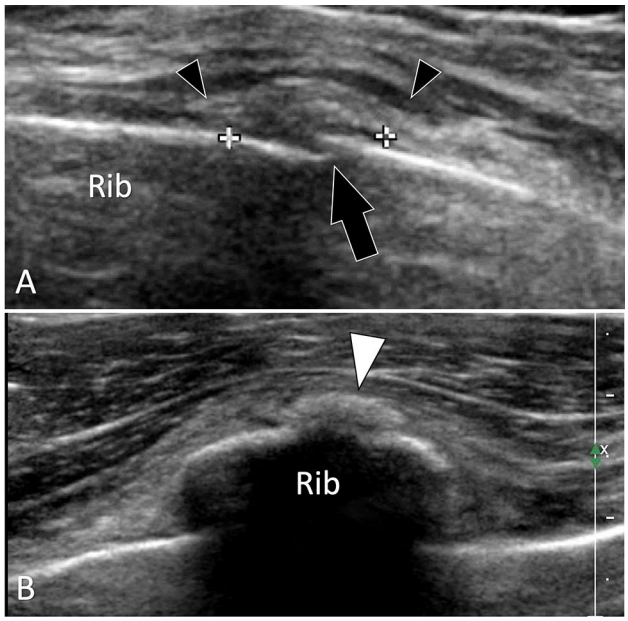

Fig. 12 Occult acute fractures. Rib fracture. **a, b** Longitudinal (**a**) and axial **b** oblique sonograms obtained over the ninth rib. In **a,** US depicts a focal interruption (black arrow) of the external cortex of the rib compatible with a minimally displaced fracture. Note thickening of the periosteum (callipers) and swelling of the local soft tissues (black arrowheads). In **b**, early callus formation appears as a small hyperechoic area (white arrowhead)

involved. Due to the local complex anatomy, radiographs are limited in displaying non-displaced fractures. US can show fractures in patients with post-traumatic persisting pain examined for soft-tissue assessment.

Scaphoid Scaphoid fractures account for 70% of carpal bone fractures [51], but may be missed on the initial radiographs in up to 25% of cases. They must be promptly recognised to avoid non-union and secondary degenerative joint changes. Several articles reported the utility of US in detecting scaphoid fractures [52–54]. The sensitivity and specificity of US in the assessment of scaphoid fracture was evaluated at 92% and 71% with a positive predictive value of 46% and a negative predictive value of 97% [52]. Fractures can also affect the palmar tubercle of the scaphoid (Fig. 13). These fractures can mimic post-traumatic tendinopathy of the flexor carpi radialis tendon or sprain of the scaphoid–trapezio-trapezoid joint [36, 55]. These fractures can be well imaged by US, which can additionally assess the flexor carpi radialis tendon [55].

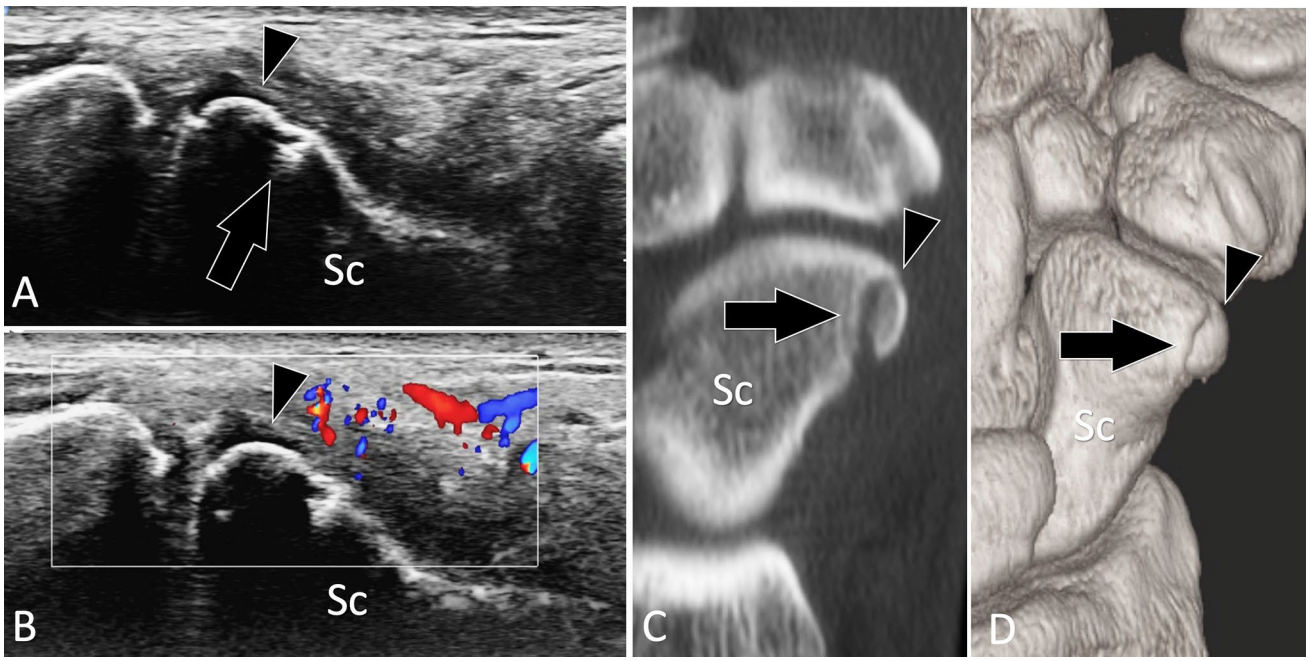

Fig. 13 Occult acute fractures. Scaphoid tubercle fracture. a, b Conventional (**a**) and colour Doppler (**b**) sagittal oblique US obtained over the palmar aspect of the scaphoid (Sc). **c**, **d** sagittal 2D (**c**) and 3D (**d**) reconstructed CT of the wrist. Previous standard radiographs were normal. In **a** US shows a non-displaced fracture (arrow) of the scaphoid tubercle which appears as a small fragment (arrowhead). In **b,** note local hyperaemia at colour Doppler. **c**, **d** CT confirmed the US findings

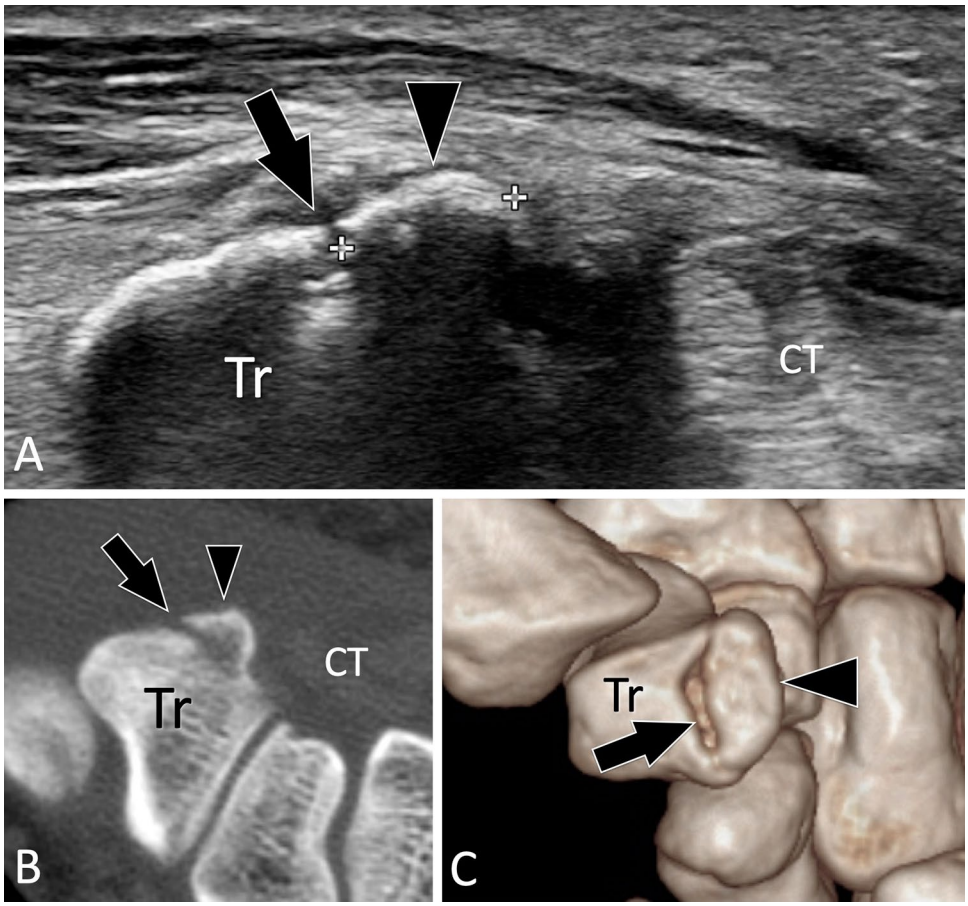

Fig. 14 Occult acute fractures. Trapezium tubercle fracture. **a** Axial US obtained over the palmar aspect of the trapezium (Tr). **c**, **d** Axial native (**c**) and 3D (**d**) reconstructed CT of the wrist. Previous standard radiographs were normal. In **a,** US shows a non-displaced fracture (arrow) of the tubercle of the trapezium which appears as a small fragment (arrowhead). **c**, **d** CT confirmed the US findings

Hamate Kato et al., in a retrospective analysis of 16 patients with fracture of the HH proven by CT, found that the fracture was visible at X-ray in only 31% of patients [56]. If undiagnosed, HH fractures can evolve towards a painful pseudo arthrosis or can injure the small finger flexor tendons, ulnar nerve, or ulnar artery branches [57, 58]. US can detect HH fracture if a special technique of examination is used [27]. US can also differentiate a fracture from non-fusion of the ossifying nucleus of the HH, a condition known as os hamuli proprium [18].

Trapezium Fractures of the tubercle of the trapezium are rarely diagnosed by radiographs, since the carpal tunnel view, the only view that can detect them, is difficult to obtain in traumatised patients. US can detect and assess such fractures (Fig. 14) [59].

Sesamoid bones Sesamoids are small ossicles found inside the periarticular tendons. They increase the effectiveness of tendons and prevent excessive overload. Fractures of metacarpophalangeal joint thumb sesamoids follow hyperextension traumas. A high degree of suspicion is necessary to detect them on X-ray because of the size of sesamoids and their superposition on the first metacarpal head [60]. US shows cortex discontinuity with local inflammatory changes and tenderness via US-guided palpation [61, 62]. In addition, associated injuries of the

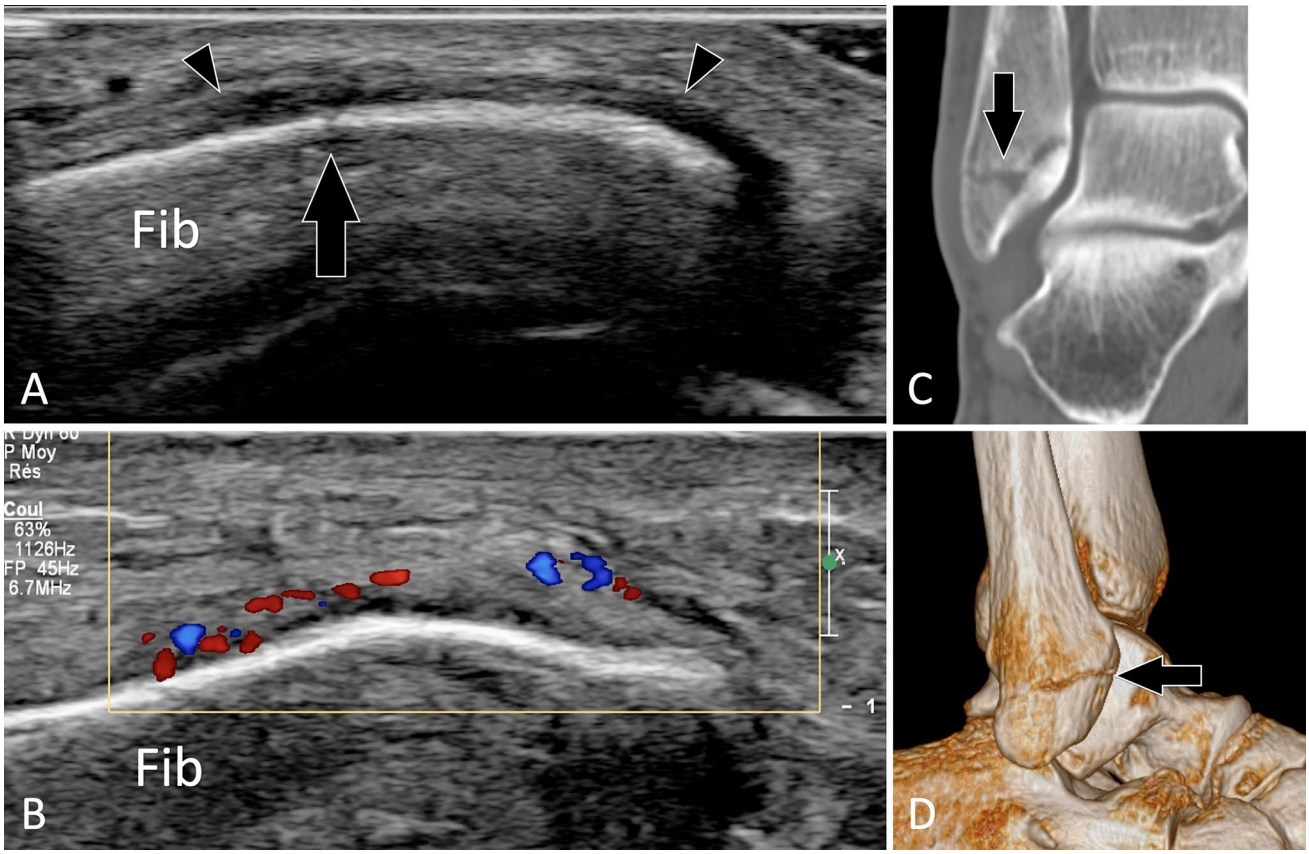

Fig. 15 Occult acute fractures. Peroneal malleolus fracture. **a**, **b** Conventional (**a**) and colour Doppler (**b**) coronal US obtained over the inferior fibula (Fib). **c**, **d** Coronal 2D (**c**) and 3D (**d**) reconstructed CT of the ankle. Previous standard radiographs were normal. **a** US shows an non-displaced fracture (arrow) of the fibula and hypoechoic thickening of the periosteum (arrowheads) that shows hypervascular changes at colour Doppler (**b**). **c**, **d** CT confirmed the US findings

MCP collateral ligaments or palmar plate can be demonstrated [61, 62].

Lower limb

Femoral fractures are diagnosed with radiographs, while CT enables an optimal detection of the number and positions of fragments in the pre-surgical scenario. US has no role in the diagnosis of femoral fractures. US findings in fractures of the patella [36, 63], tibia [64], and malleoli [65] (Fig. 15) have been described.

In the foot [66], US can detect AF, including the lateral process of the talus [35], anterosuperior process of the calcaneus [67], and the cuboid and the base 5th metatarsal [68, 69]. Sonologists must be aware that US can detect these fractures and must assess bones in patients with sprained ankles.

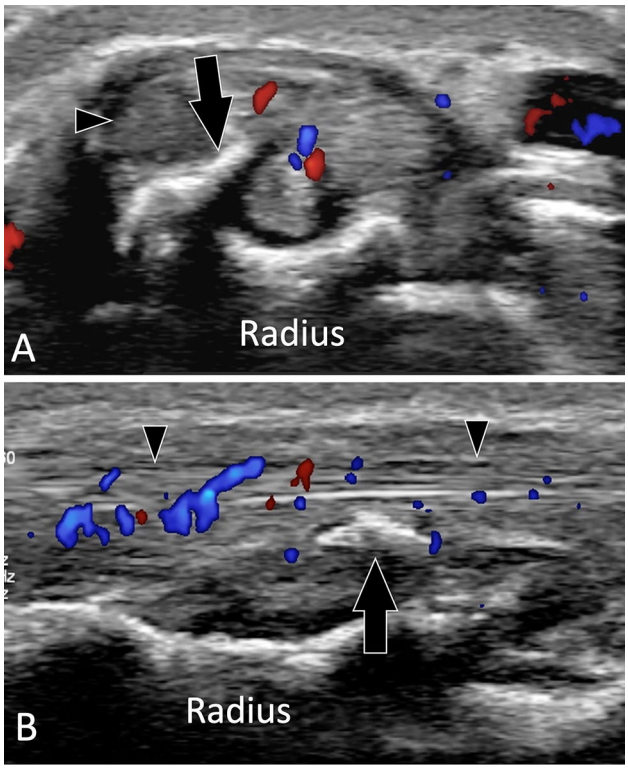

Fig. 16 Complications of fractures. Tendons lesions. **a**, **b** Axial (**a**) and sagittal **b** colour Doppler in a patient with the previous fracture of the distal epiphysis of the radius. Images show irregularity of the dorsal aspect of the radius with a local beak-like appearance (arrows). The adjacent extensor tendons (arrowheads) are irregular and inflamed secondary to impingement of the aggressive bone

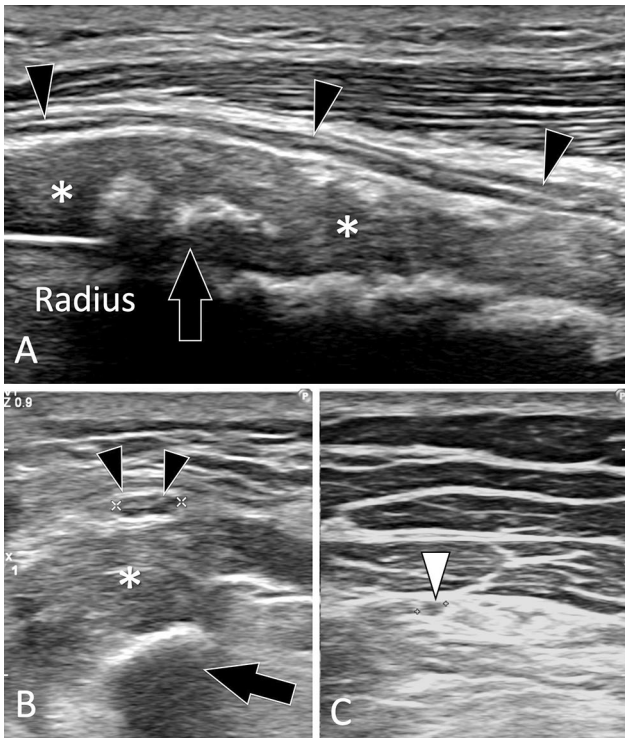

Fig. 17 Complications of fractures. Nerves lesions. **a**, **c** Sagittal (**a**) and axial (**b**, **c**) sonograms in a patient with the previous fracture of the radius shaft. In **a** the superficial branch of the radial nerve (black arrowheads) is hypoechoic and thickened. The nerve is displaced by bone callus (asterisks) which is partially calcified. In **b,** note the swelling (black arrowheads 3.5 mm) of the nerve in the axial plane compared with the nerve (white arrowhead 1.6 mm) imaged at a more distal level (**c**)

US and callus formation

US can detect the early callus formation and non-union [37, 38, 70]. Several stages were described in fracture healing [71]. First, a haematoma can be detected between the two bone ends, followed by soft callus and progressive calcifications until osseous union. Colour Doppler helps with the evaluation of vascular invasion of the early callus. High vascularity beyond 3 months is associated with delayed union.

Complications of fractures

Tendon lesions

Tendons can be injured in acute fractures, but are most frequently damaged secondary to impingement on the irregular bone surfaces after fracture healing. This is mostly seen at the wrists, where extensor tendons run over the dorsal cortex of the radius and ulna [72] (Fig. 16). Local impingement causes tenosynovitis, and partial and complete tears. US-guided injection of steroids/anaesthetics can be performed as a first-line treatment in tenosynovitis. Surgical resection of the bone spur and eventually a tenodesis in tendon rupture is the treatment of choice if the injection is ineffective or only temporarily effective.

Nerve lesions

Acute nerves injuries can be associated with fractures if the nerve runs close to the bone [73]. A typical example is radial nerve injuries associated with fractures of the mid-shaft of the humerus [74]. During fracture, healing nerves can be displaced/stretched by the callus or entrapped inside it (Fig. 17). US shows the thickening and hypo-echogenicity of the nerve as well as its relation with the callus.

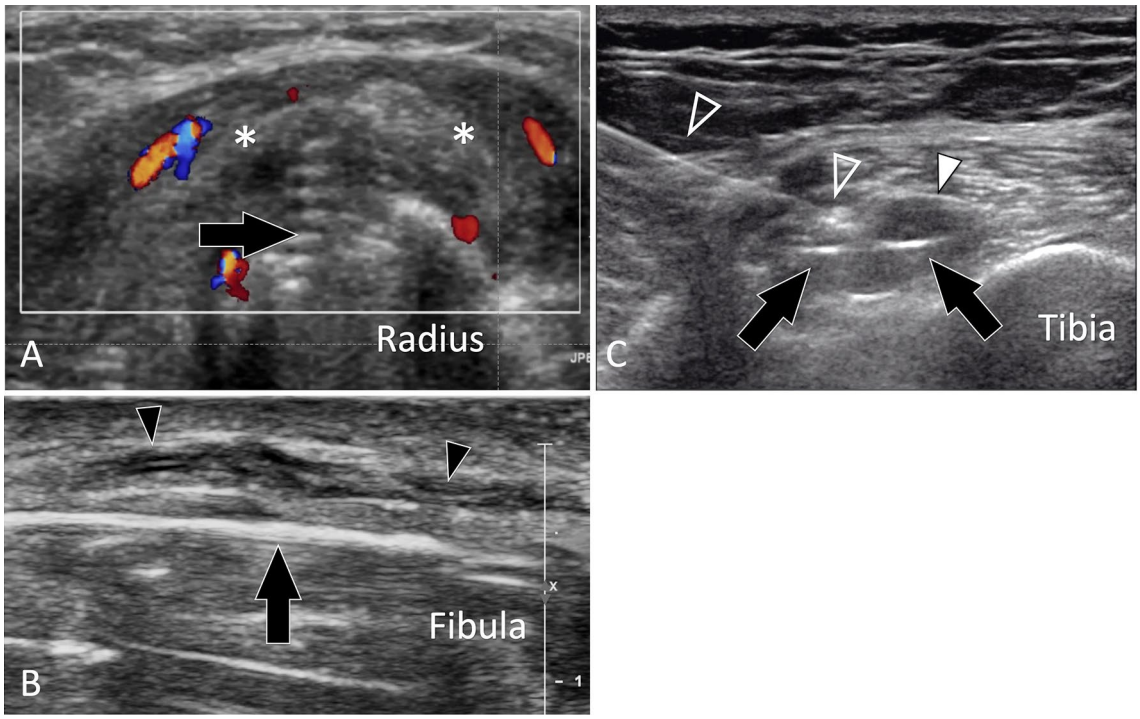

Fig. 18 Complications of fractures. Postsurgical complications. **a** Axial sonogram in a patient with the previous fracture of the radius shaft treated by an osteosynthesis plate. A screw's tip (black arrow) can be seen protruding from the surface of the bone cortex. Note swelling, oedema (asterisks), and hypervascular changes in the soft tissues surrounding the screw due to local impingement. **b** Longitudinal US images obtained over the lateral aspect of the inferior fibula in a patient with local fracture treated by an osteosynthesis plate. US images the surgical plate (black arrow). Note that the superficial branch of the fibular nerve (black arrowheads) is hypoechoic and thickened because of trauma during recent surgery. **c** Axial sonogram obtained over the proximal metaphysis in a patient with previous arthroscopic surgery for ACL tear. The screw inside the tibial tunnel (arrows) protrudes from the bone cortex and causes local bursitis (white arrowhead) and pain to local pressure. To confirm the origin of the patient's pain, a US-guided anaesthetic injection was performed. Note the needle (void arrowheads) inserted under real-time scanning the tip of the needle is in contact with the screw

Postsurgical complications

US is accurate in assessing the impingement of soft tissues against orthopaedic hardware (OH) (Fig. 18). The main advantage of US compared to MRI is the absence of metal artefacts that limit MRI assessment. Compared with CT, US allows a better evaluation of soft tissue [75, 76]. US detects orthopaedic hardware as a hyperechoic structure with posterior artefacts. Screw tips are prone to injury the adjacent soft tissues, because the sharp cutting thread appears as multiple oblique parallel hyperechoic lines [75]. US assesses the relationship between OH and the adjacent structures, the presence of collections, and hyperaemia on the colour Doppler or tears. Painful local compression, under US guidance, over the orthopaedic hardware confirms that this is responsible for the symptoms. In selected cases, a US-guided injection of lidocaine at the interface between the OH and local soft tissues is requested by the surgeon as an anaesthetic test.

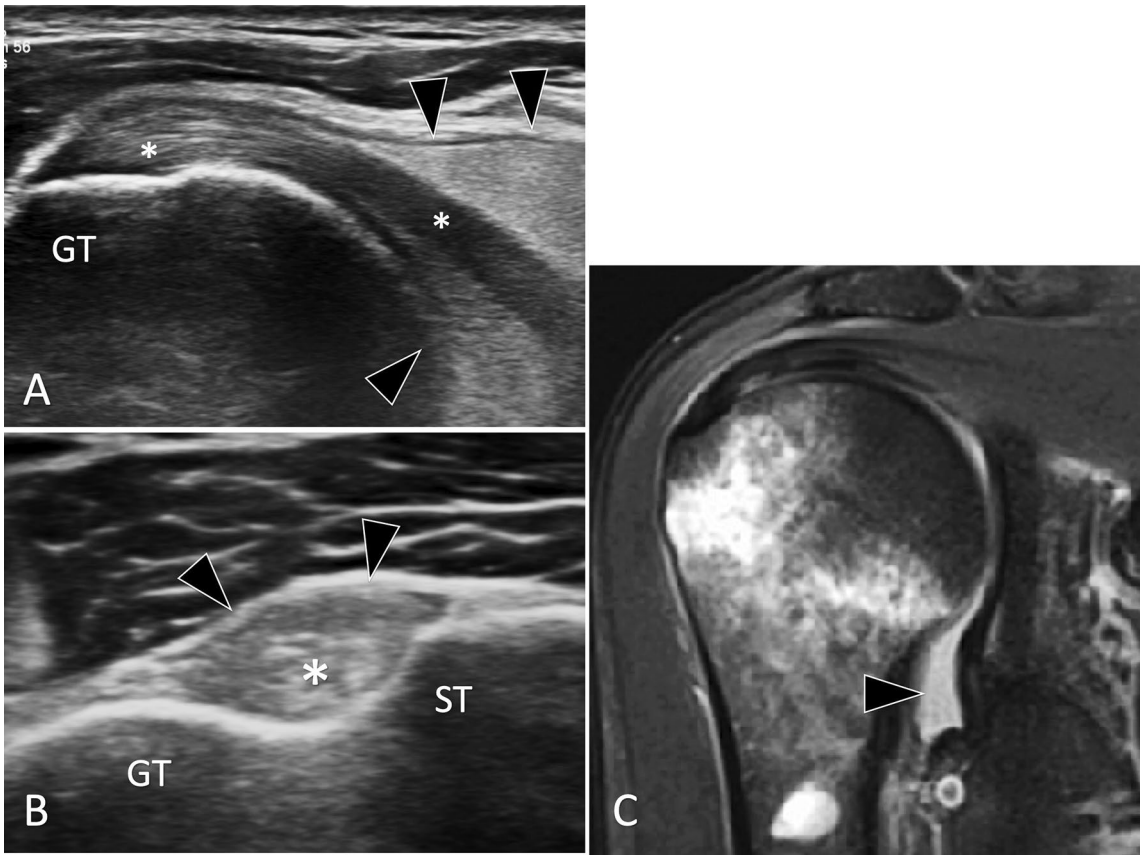

Fig. 19 Intra-articular fractures: haemarthrosis. **a**, **b** Longitudinal (**a**) and axial (**b**) sonograms on the long head of the biceps tendon obtained over its intra-articular (**a**) and extra-articular (**b**) portion. Images were acquired in a patient with post-traumatic shoulder and negative radiographs. **c** Coronal oblique T2-weighted MR image. US shows a normal biceps tendon (asterisks). The tendon is surrounded by a hyperechoic intra-articular effusion (arrowheads) suggesting a haemarthrosis. Since no fractures were detected by US, MRI was performed (**c**) and showed a "in situ" fracture of the surgical neck of the humerus and confirmed haemarthrosis (arrowhead)

Intra-articular fractures

Intra-articular fractures are associated with a joint effusion and carry a high degree of complications, even if minimally displaced. The effusion can be composed of blood (haemarthrosis) or blood mixed with yellow marrow (lipohaemarthrosis). Horizontal bean X-ray can detect lipohaemarthrosis by showing fat floating on the blood effusion. Haemarthrosis appears at US a hyperechoic homogeneous articular effusion (Fig. 19). In vitro [77] and in vivo US allow detection of lipohaemarthrosis [77–79] (Fig. 20). The US detection of haemarthrosis/lipohaemarthrosis must stimulate a careful US evaluation of articular surfaces to detect possible occult fractures. If a fracture is not found in symptomatic patients, a CT or MRI must be performed.

US can appreciate Hill–Sachs fractures (Fig. 21) [80], Freiberg disease (Fig. 22), osteochondral injury, and osteochondral fragments (Fig. 23) [81, 82].

Bone avulsions

Bone avulsions are traumatic cortical detachments at the insertion of tendons or ligaments due to a pulling force. US can detect the avulsed fragment and prove its connection

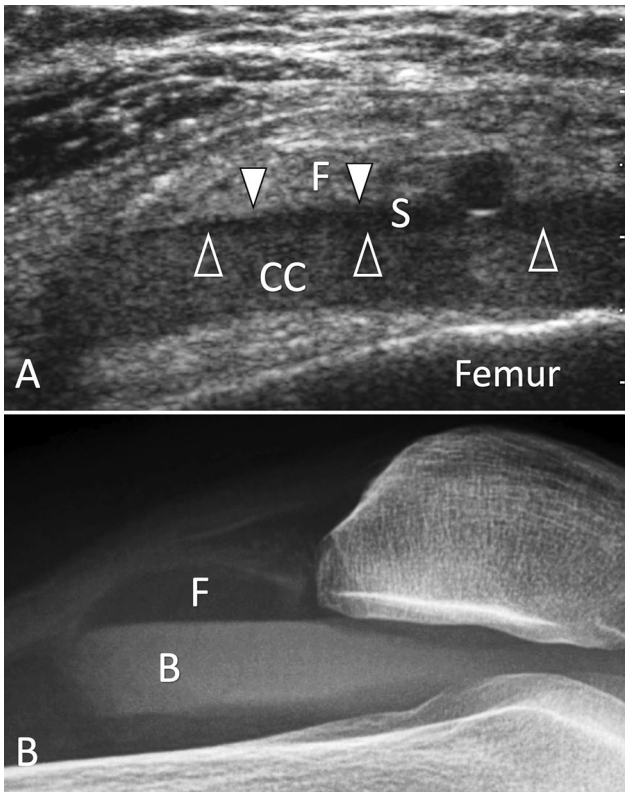

Fig. 20 Intra-articular fractures. Lipohaemarthrosis. **a** Sagittal sonogram on the suprapatellar recess obtained in a patient with post-traumatic knee effusion and pain with negative radiographs. **b** Horizontal bean radiograph. In note **a**, the presence of an effusion inside the suprapatellar recess presenting a three-layered appearance separated by two fluid–fluid levels (arrowheads). The superior layer is hyperechoic and corresponds to fat (F) and the thin middle hypoechoic layer corresponds to serum (S), while the deep layer is due to sedimentation of cells content (CC). Radiograph (B) confirms the presence of intra-synovial fat (F) floating on blood (B), but cannot visualise the serum content. CT (not shown) showed an occult non-displaced fracture of the tibial plateau

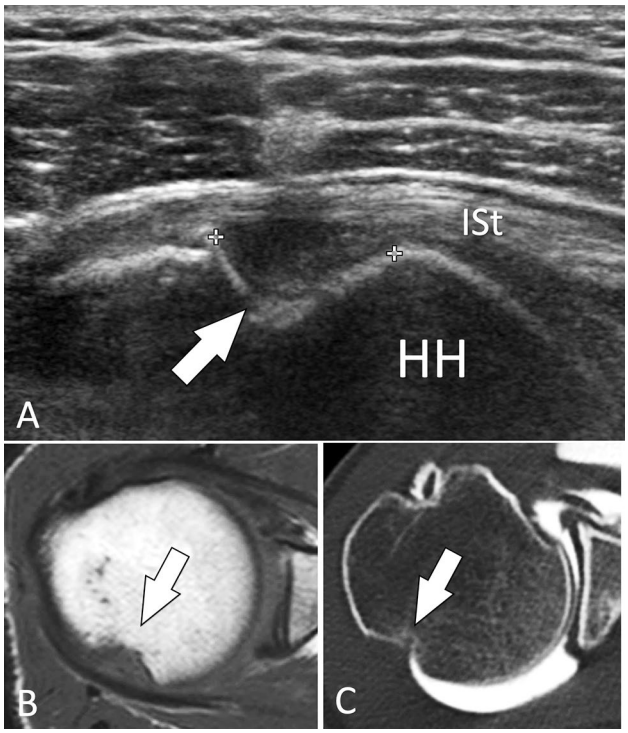

Fig. 21 Intra-articular fractures. Hill–Sachs fracture. **a** Axial sonogram on the posterior aspect of the humeral head (HH) obtained in a patient with the previous anterior shoulder luxation. **b**, **c** Axial T1-weighted (**b**) and axial CT arthrogram (**c**). In **a,** US shows the fracture impaction (arrow) of the head at the level of the superior infraspinatus tendon (ISt). MRI and CT arthrography in the same patient confirm the US findings

with the tendon or ligament. Local inflammation and pain at local pressure are found in acute cases. Examples of bone avulsion detectable by US at the upper extremity are: dorsal cortical avulsion of the triquetrum, avulsion at the distal end of the collateral ligament of the MCP joint in gamekeeper thumb (Fig. 24), palmar plate avulsion (Fig. 25), avulsion of the flexor tendons or extensor apparatus of the fingers (Jersey finger) [83], and mallet finger. At the lower extremity, US can detect bone avulsion of the ischial tuberosity (Fig. 26) [84], insertion of the rectus femoris [85], tibialis posterior (Fig. 27), peroneus longus (Fig. 28) [86, 87], and anterior talofibular ligament (Fig. 29).

Stress fractures

General considerations and US findings

Stress fractures (SFs) can be divided into fatigue (FSFs) and insufficiency fractures (ISFs) depending on whether they result from an abnormal load to a normal bone or a normal load on a weak bone [88].

Lower extremity FSFs are the most frequent in sport activities [89] with an incidence of over 95% [90]. In a

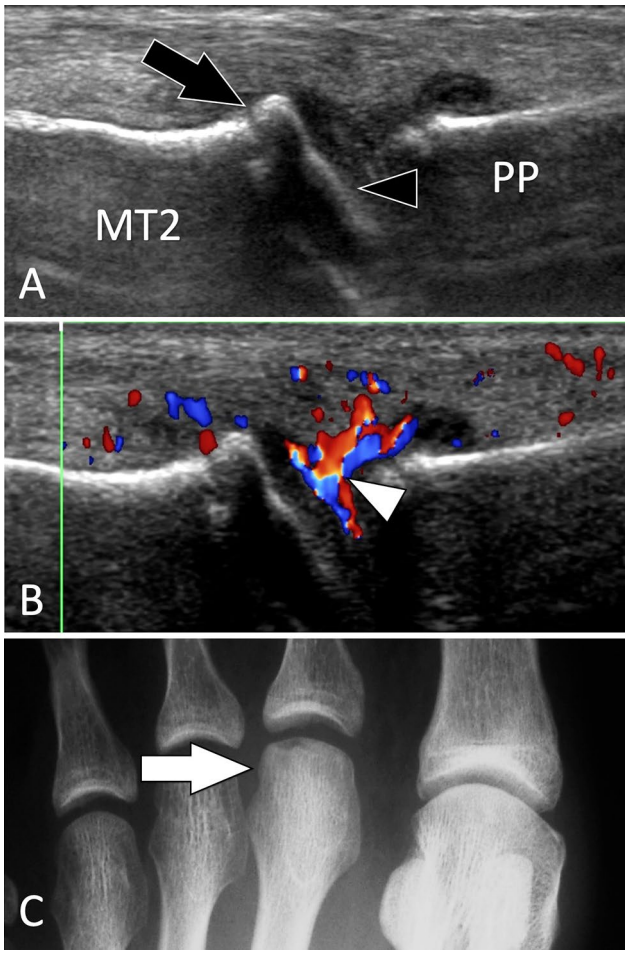

Fig. 22 Intra-articular fractures. Freiberg disease. Sagittal conventional (**a**) and sagittal colour Doppler (**b**) sonograms on the dorsal aspect of the second metatarsophalangeal joint. **c** A-P radiograph. Sonograms illustrate a flattened joint surface (black arrowhead) associated with a small dorsal osteophyte of the second metatarsal (MT2). In **b,** note synovial hypertrophy with hyperaemia (white arrowhead). Radiograph shows a dense head of the metatarsal with a slightly fat articular surface

study of 320 bone scan-positive stress fractures, the most frequently injured bone was the tibia (49.1%), followed by the tarsals (25.3%), metatarsals (8.8%), femur (7.2%), fibula (6.6%), pelvis (1.6%), sesamoids (0.9%), and spine (0.6%) [91]. Patients with FSFs are classically high-level sportsmen enrolled in competitions [91, 92]. Recently, with the increase in the age of the population and the higher frequency of "weekend sports", FSFs are more widely observed in the general population.

ISFs result from normal loading upon abnormally weakened bones [93]. They mostly affect aged patients with primary or secondary osteoporosis, such as patients with corticosteroid or metabolic bone diseases, rheumatoid arthritis, and neurological disorders. ISFs affect mostly the sacrum and pelvis, femoral neck, or subchondral regions of the knee, calcaneum, and metatarsals.

Although the location of FSFs and ISFs is different, the clinical appearance is similar. Patients present with local mechanical pain associated with local soft-tissue swelling. The clinical diagnosis of an SF is based on the history and clinical findings, but an imaging technique is almost always required to confirm the suspicion. Treatment consists of rest, non-weight-bearing, and NSAIDs.

Imaging assessment of SF classically relies on standard radiographs, CT, MRI, and bone scans, depending on the anatomic region and clinical scenario. Standard radiographs are often negative initially [88, 94]. Computed tomography scans (CT scans) are usually obtained in longitudinal fractures of the tibia, but have a low sensitivity compared with MRI. Bone scintigraphy is very sensitive, but is aspecific. MRI is the imaging gold standard for the early detection of SF, but is not always available and expensive. In SF, US detects changes to soft tissues, the periosteum, and the bone cortex. Soft-tissue oedema appears on US as an ill-defined hyperechoic area. Its detection must encourage examination of the bone surfaces, in particular assessing whether the local tendons are normal. Thickening of the periosteum appears to be hypoechoic thin band located over the bone cortex. The vessels of the inflamed periosteum can be visualised by colour Doppler. Attention must be made to avoid excessive pressure through the transducer to prevent vessel compression. Frequently, the cortical surface shows small irregularities. It must be noted that changes in the periosteum and cortex can be very subtle in early SFs. Although the overall US appearance strongly suggests an SF, it must be stressed that the US findings are aspecific and the US appearance needs to be correlated to clinical data.

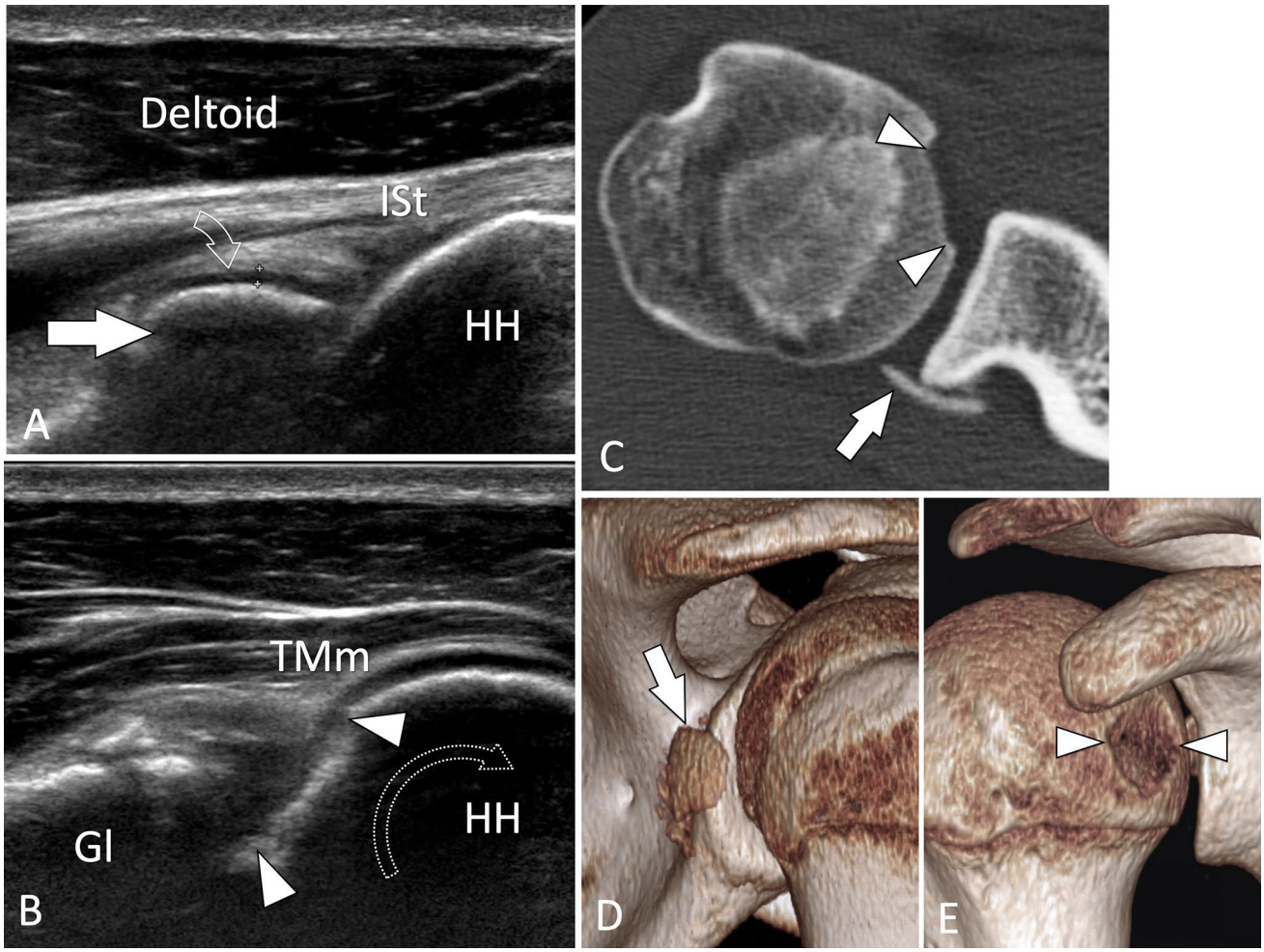

Fig. 23 Intra-articular fractures. Osteochondral injury and osteochondral fragments. **a**, **b** Axial conventional sonograms on the dorsal aspect of the humeral head (HH) obtained (A) at the level of the infraspinatus tendon (ISt) and **b** in a more inferior position during maximal internal rotation (curved arrow) of the arm. **c** Axial native CT image, **d**, **e** 3D reconstructed CT images. In **a**, an intra-articular osteochondral fragment (white arrow) is depicted at the posterior joint space. Note the hyaline cartilage (curved arrow) at the surface of the fragment that has a convex shape. In **b,** the nidus of the fragment depicts a defect in the joint surface (arrowheads). *TMm* teres minor muscle, *Gl* glena. *C-E* CT confirms the US appearance

Specific location

Knee region: femur condyles and proximal tibia SFs of the femoral condyles and proximal epiphysis of the tibia are mainly due to local overload, such as in malalignment of the lower extremities or complete tears of a meniscal root. MRI is the imaging technique of choice. The US appearance of SFs of femoral condyles (Fig. 30) is very similar to that of osteonecrosis and differentiation is not achievable by US. Nevertheless, US can play a role in addressing the patient for further evaluation with MRI, since it excludes soft-tissue disorders and focuses attention on the bone. The appearance

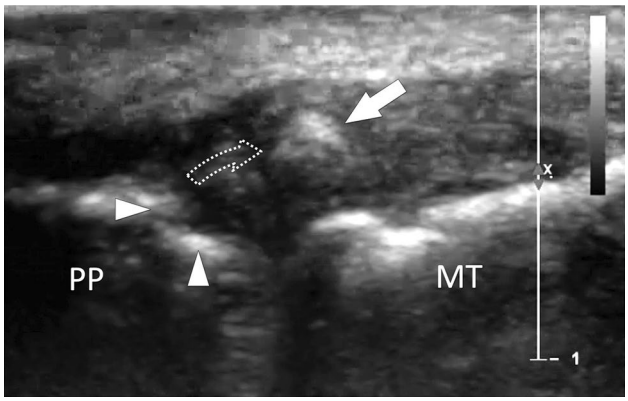

Fig. 24 Bone avulsion. Gamekeeper's thumb. **a** Coronal oblique conventional sonogram obtained on the ulnar aspect of the metacarpophalangeal joint of the thumb in a patient with gamekeeper's thumb. Image shows a bone avulsion (white arrow) resulting from a retraction (dotted curved arrow) of a fracture avulsion of the base (white arrowheads) of the proximal phalanx (PP). US can appreciate both the size of the avulsed fragment and then the entity of the proximal retraction. *MT* first metatarsal

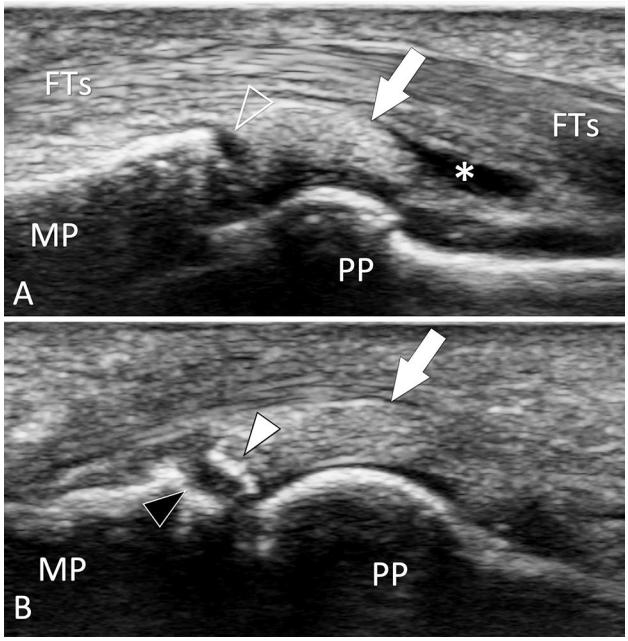

Fig. 25 Bone avulsion. Palmar plate. **a**, **b** Sagittal conventional sonograms obtained on the palmar aspect of the proximal inter-phalangeal joint of the third finger in a patient with previous joint sprain. In **a,** the palmar plate (white arrow) is detached (void arrowhead) from the base of the middle phalanx (MP). Note a fluid effusion (asterisk) inside the palmar proximal joint recess. In a slightly more medial image (**b**), a cortical fragment (white arrowhead) avulsed from the base (black arrowhead) of the proximal phalanx is evident. US can appreciate both the size of the avulsed fragment and then the entity of the proximal retraction. *PP* proximal phalanx, *FTs* flexor digitorum tendons

of tibial epiphysis SFs is similar. SF of the tibial proximal metaphysis can be misinterpreted as pes anserinus tendinitis. Bilateral simultaneous involvement is rare [95].

Tibial shaft Fractures of the tibial shaft mostly affect athletes, especially runners. Their typical location is the anteromedial aspect of the distal third of the tibia [96, 97] (Fig. 31). Most fractures are suspected clinically due to the mechanical pain and location. The US examination is pointed to the area of maximal tenderness and compared with the contralateral side. Changes are frequently subtle particularly when the patient is seen early.

Malleoli Bianchi et al. reported a retrospective study of six patients (4 women and 2 men, age range of 24–52 years, and mean age of 39 years) in which US diagnosed an SF of the ankle malleoli [98]. In all patients, the diagnosis was not suspected clinically and US was obtained to evaluate soft tissues. Sonologists must be aware of the US appearance of malleoli SF and should include this condition in the differential diagnosis of mechanical perimalleolar pain.

Calcaneus Both FSFs and ISFs can affect the calcaneus [99, 100]. Fractures are mainly located at the posterior third of the bone, i.e., the site of maximal load during weight bear-

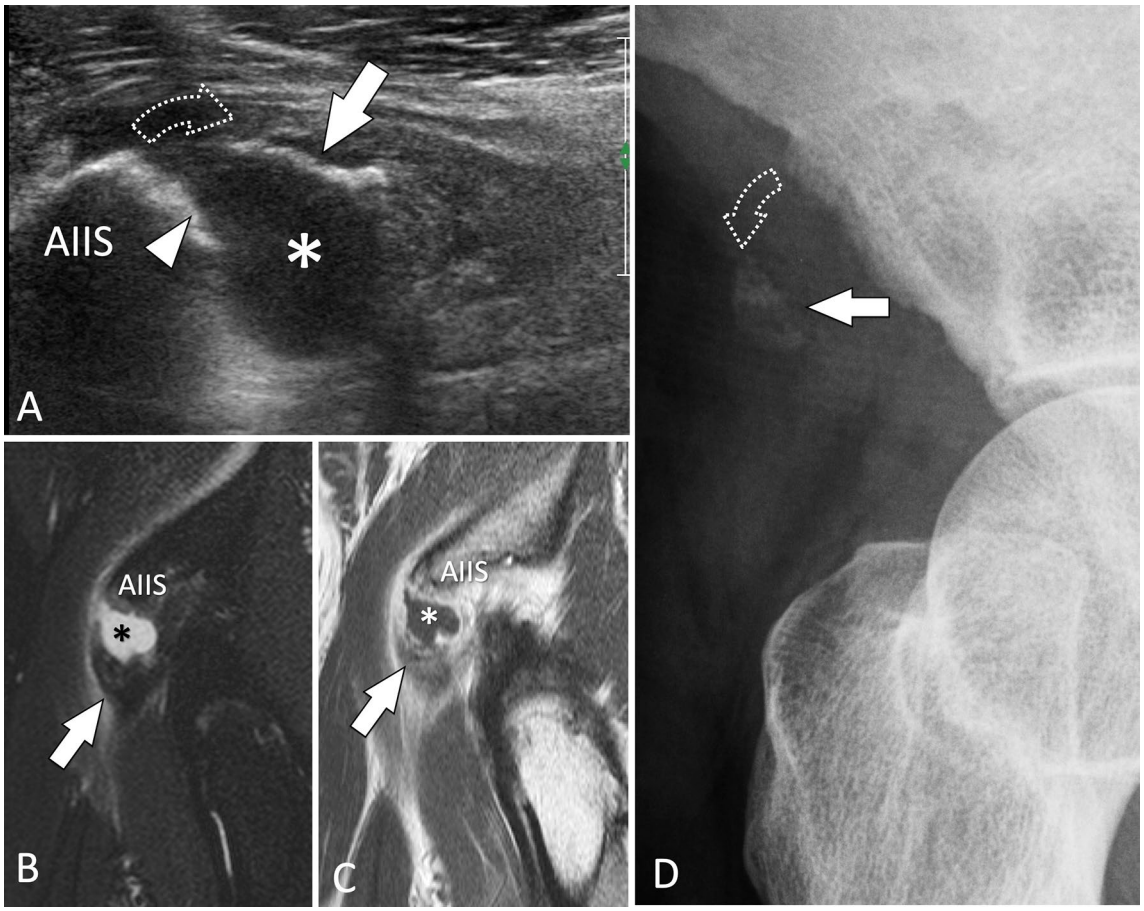

Fig. 26 Bone avulsion. Rectus femoris tendon. **a** Sagittal sonogram obtained on the anterior inferior iliac spine (AIIS) shows avulsion (dotted arrow) of a bone fragment (white arrow) from the AIIS which shows irregularity of its surface (white arrowhead). The asterisk points to a local hematoma. **b**, **d** STIR (**b**) and T1-weighted post-injection (**c**) confirm the US findings. **d** Anterior oblique standard radiographs

ing (Fig. 32) [101]. Calcaneal FSFs are mainly seen in sedentary patients that increase physical activity and do not respect a schedule. Calcaneal ISFs are typically seen in aged females affected by osteoporosis. The clinical signs are the same for FSFs, i.e., mechanical pain associated with local oedema. In these patients, US is frequently the first examination demanded to exclude tendinopathy [100].

OS peroneum SF of the os peroneum (OP), a sesamoid bone located inside the peroneus longus tendon, is one of the causes of painful os peroneum syndrome. When subject to excessive chronic overload, the OP displays internal oedema, followed by an SF and its possible displacement associated with the proximal migration of the posterior fragment [86, 87]. Patients present with mecha-

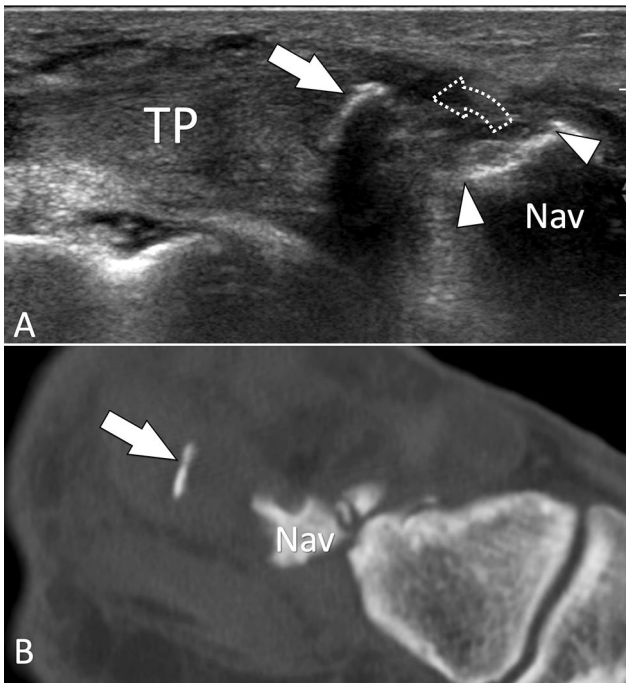

Fig. 27 Bone avulsion. Tibialis posterior tendon. **a** Sagittal sonogram obtained on the distal insertion of the tibialis posterior tendon (TP) shows avulsion (dotted arrow) of a thin bone fragment (white arrow) from the navicular bone (Nav). Note the defect in the surface of the navicular (white arrowheads). **b** Corresponding "D reconstructed sagittal CT image confirms the US findings

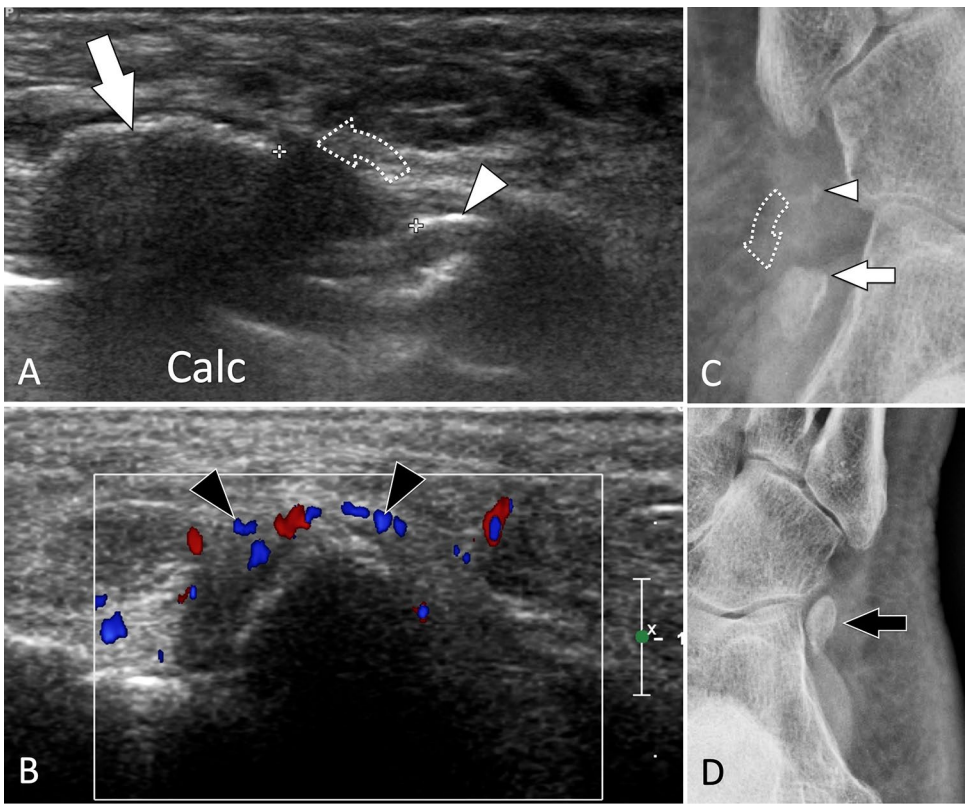

Fig. 28 Bone avulsion. Os peroneum. **a**, **b** Axial oblique conventional (**a**) and coronal oblique colour Doppler (**b**) sonograms obtained on the Os peroneum in a patient with recent trauma. Images show a fracture of the ossicle with the presence of a proximal large (white arrow) and a small distal (white arrowhead) fragment. Note proximal displacement (dotted arrow) of the proximal fragment due to traction through the peroneus longus tendon. **b** Colour Doppler shows local hyperaemia (black arrowheads). **c**, **d** Internal oblique radiographs of the affected (**c**) and contralateral (**d**) foot. In **c,** note the fracture avulsion of the upper pole of the os peroneum associated with proximal displacement confirming the US appearance. **d** A normal os peroneum

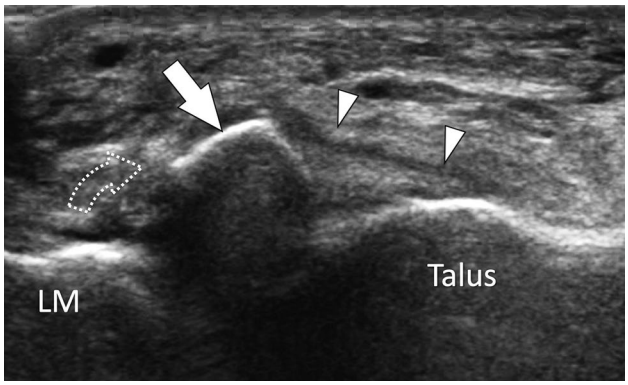

Fig. 29 Bone avulsion. Anterior talofibular ligament. Axial oblique sonogram obtained on the talofibular ligament (white arrowheads) shows avulsion of the anteroinferior lateral malleolus (LM) with presence of a displaced (dotted arrow) fragment (white arrow)

nical pain located at the lateral cuboid region. Upon US, oedema surrounding the OP and the peroneus longus tendon is evident (Fig. 33). The OP presents hypervascular changes on colour Doppler, sometimes associated with similar changes to the cuboid. Displacement of the fracture with proximal migration of a bone fragment can be easily appreciated by US and is confirmed by comparison to the contralateral side. In addition, an US-guided local steroid injection can be helpful in relieving pain [102].

Metatarsals Due to their high frequency, the US appearance of metatarsal SFs affecting the distal metaphysis received the early attention [103–107]. One of the clinical landmarks of metatarsal SFs is the soft-tissue oedema of the dorsum of the foot associated with local pain. The US appearance is the same for the other SFs, including irregularity of the cortex, thickening of the periosteum local oedema, and increased vascularity (Fig. 34). An interesting additional sign is the increase in the posterior shadowing of the affected metatarsal [108]. SFs of the proximal bases of the second metatarsal are rarer, more frequently affect ballet dancers and, contrary to distal SFs, can require surgical treatment [109]. The infrequent location, as well as the less pronounced clinical and US findings, make the detection of base fractures more challenging on US.

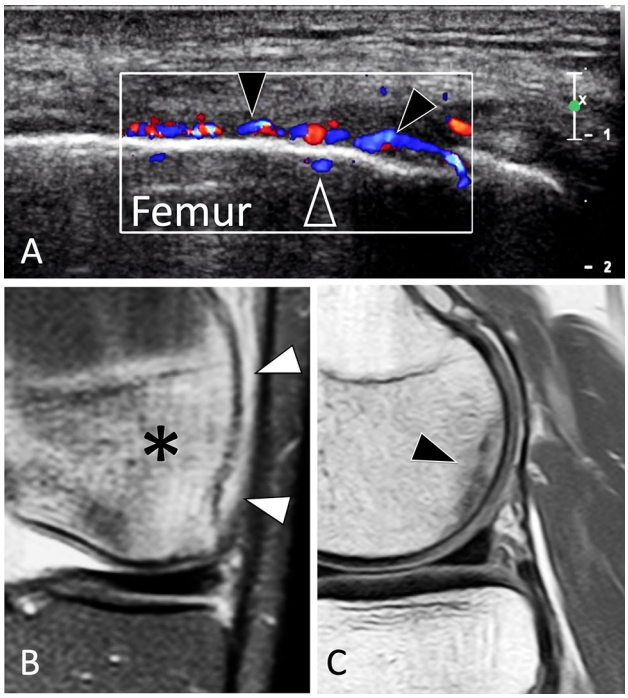

Fig. 30 Stress fracture. Femur condyle. **a** US image obtained over the lateral aspect of the knee, **b**, **c** MR images, coronal DP fat sat (**b**), and sagittal DP in a jogger with clinical suspected iliotibial band syndrome. In **a,** US shows hyperaemia of the thickened periosteum (black arrowheads) as well as intra-osseous extension of the vessels (void arrowhead). The iliotibial tract and the adjacent soft tissues were normal. MRI (**b**) images of oedema of the periosteum (white arrowheads) associated with cancellous bone oedema (asterisk). In **c**, MRI detects a stress fracture as a hypointense line (arrow) parallel to the condylar surface

Hallux sesamoids SFs of the hallux sesamoids are mainly FSFs [110] due to overload of the first ray of the foot. They appear as a thickening of the periosteum and an irregularity of the cortex. A focal break in the cortex, especially if associated with local hyperaemia on colour Doppler, suggests an SF (Fig. 35). The differential diagnosis with a bipartite sesamoid can be made by the fact that bipartite sesamoids are larger compared to the adjacent sesamoid, are mostly painless and show no local inflammation on colour Doppler. In cases of doubt, MRI and CT must be obtained for further evaluation. US is useless in diagnosing osteonecrosis of sesamoids.

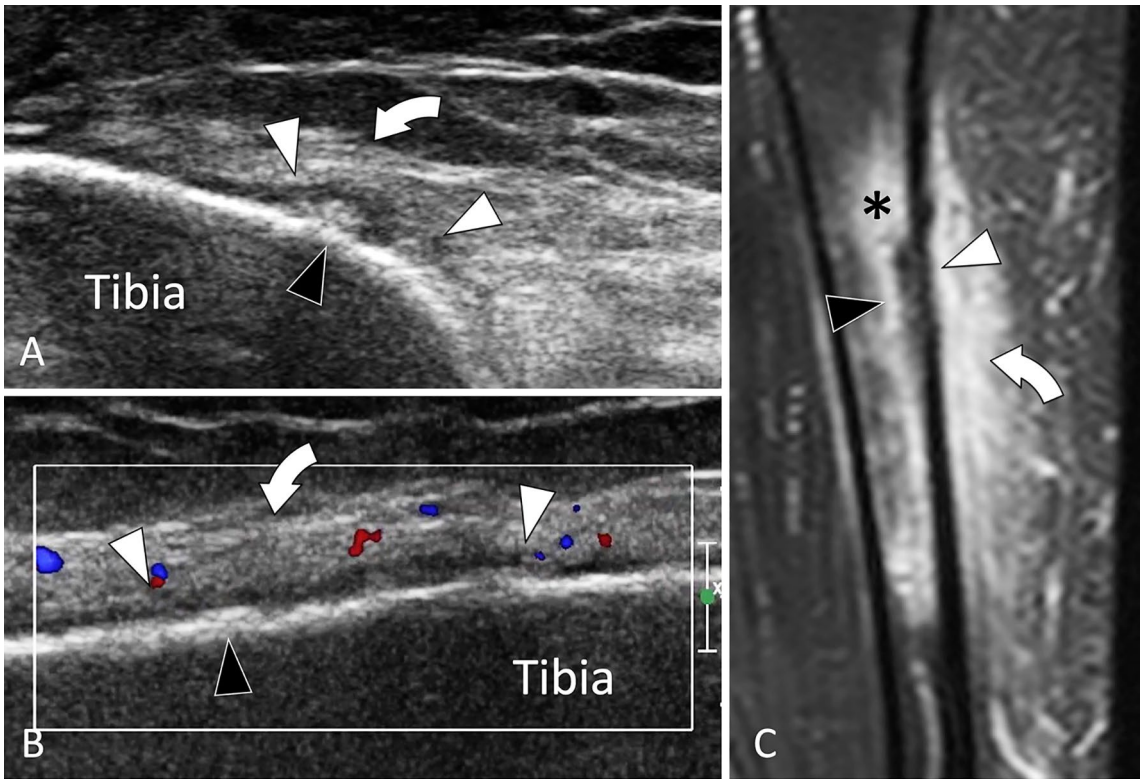

Fig. 31 Stress fracture. Tibial shaft. **a**, **b** Axial (**a**) and coronal oblique (**b**) sonograms, **d** Coronal t2-weighted fat sat MR image. Sonograms show a focal irregularity of the bone surface (black arrowheads) associated with periosteal thickening (white arrowheads) and oedema (curved arrows) of the subcutaneous soft tissues. **c** MR illustrates in a better detail oedema (asterisk) of soft tissues but also bone marrow oedema

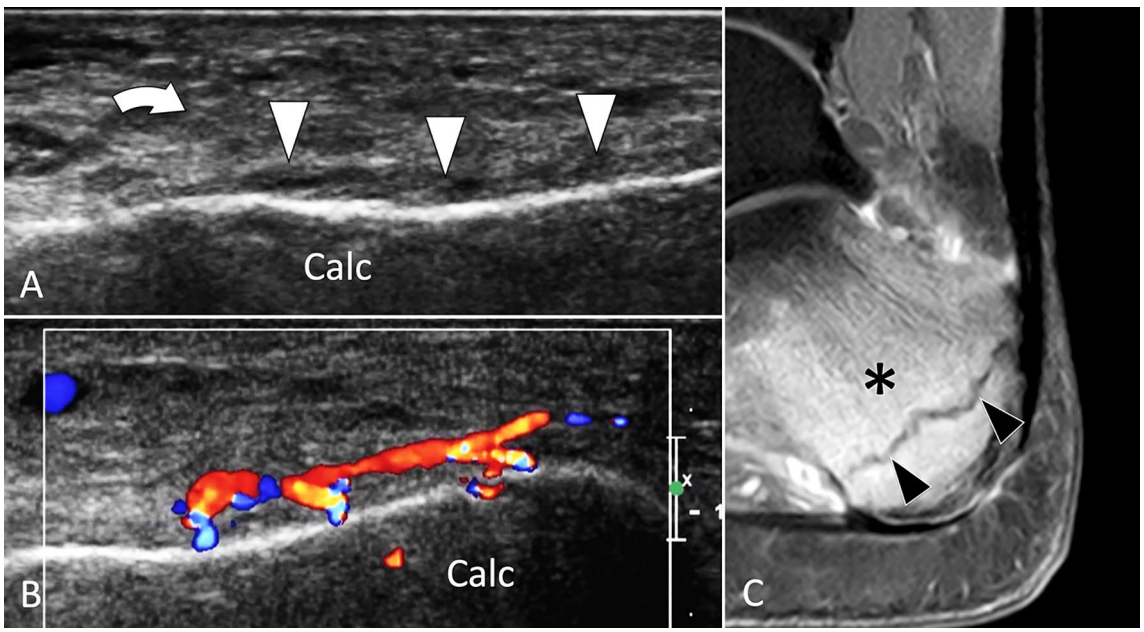

Fig. 32 Stress fracture. Calcaneum. **a**, **b** Axial oblique conventional (**a**) and colour Doppler (**b**) sonograms. **c** Sagittal T2-weighted fat sat MR image. Sonograms show periosteal thickening (white arrowheads) of the calcaneum (Calc). Note local hyperaemia at colour Doppler and associated oedema (curved arrows) of the subcutaneous soft tissues. **c** MR illustrates bone marrow oedema (asterisk) and the stress fracture as a hypointense line (black arrowheads)

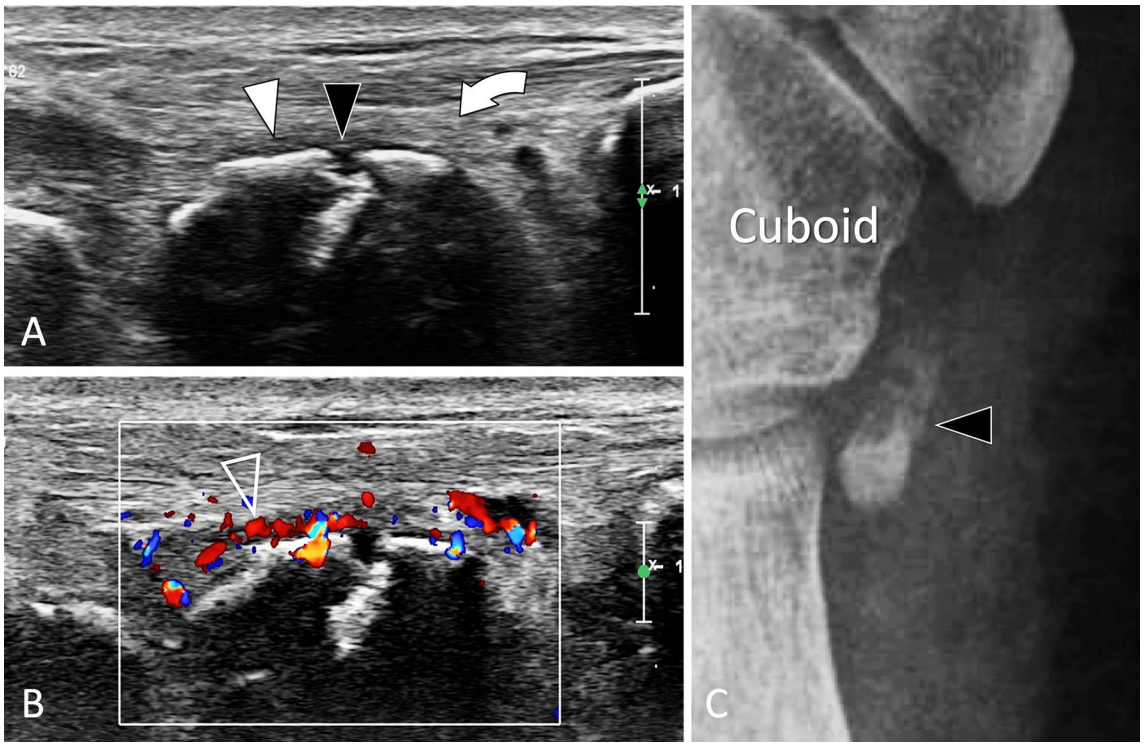

Fig. 33 Stress fracture. Os peroneum. **a**, **b** Axial oblique conventional (**a**) and colour Doppler (**b**) sonograms. **c** Internal oblique radiograph centred at the cuboid region. In **a**, **b** US shows discontinuity (black arrowhead) of the cortex of the os peroneum associated with mild periosteal thickening (white arrowhead) and associated oedema (curved arrow) of the adjacent soft tissues. The inflamed periosteum shows important hypervascular changes (void arrowhead) in **b**. Note associated oedema (curved arrows) of the subcutaneous soft tissues. In **c**, the ossicle, enlarged and irregular, presents a fracture with mild displacement. MRI (not shown) confirmed the US data showing bone marrow oedema of the ossicle and associated soft-tissue hyperaemia

Infections

US plays a complementary role in the assessment of osteomyelitis, since it cannot evaluate the cancellous bone. Nevertheless, it allows good evaluation of the extent of the infection into the local soft tissues [111]. US can detect subperiosteal effusion, especially in children, as well as abscesses (Fig. 36) and fistula in the adjacent tissues.

US can guide needle aspirations of peri-osseous collections or, in the case of infective arthritis, intra-articular effusion. Data from culture and antibiogram are imperative to choose the correct treatment.

Tumors

Osteochondromas (OCs) are the most common bone tumour (20–50% of benign bone tumours and 10–15% of all bone tumours) [112]. They are localised outgrowths of bone, in continuity with the normal cortex and medullary, covered by

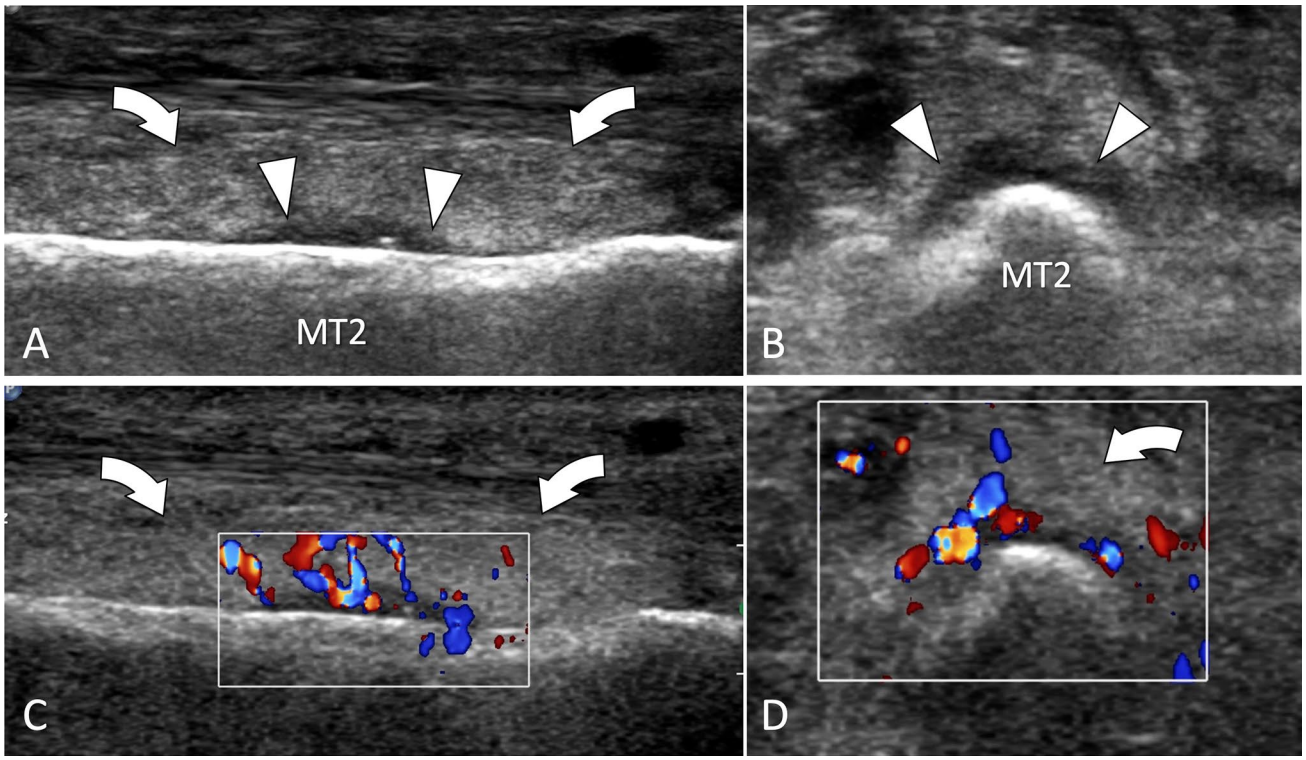

Fig. 34 Stress fracture. Metatarsal. **a**, **d** Axial and sagittal conventional (**a**, **b**) and colour Doppler (**c**, **d**) sonograms. US shows periosteal thickening (white arrowheads) of the second metatarsal (MT2). The inflamed periosteum shows important hypervascular changes in the colour Doppler images (**c**, **d**). Note associated oedema (curved arrows) of the subcutaneous soft tissues

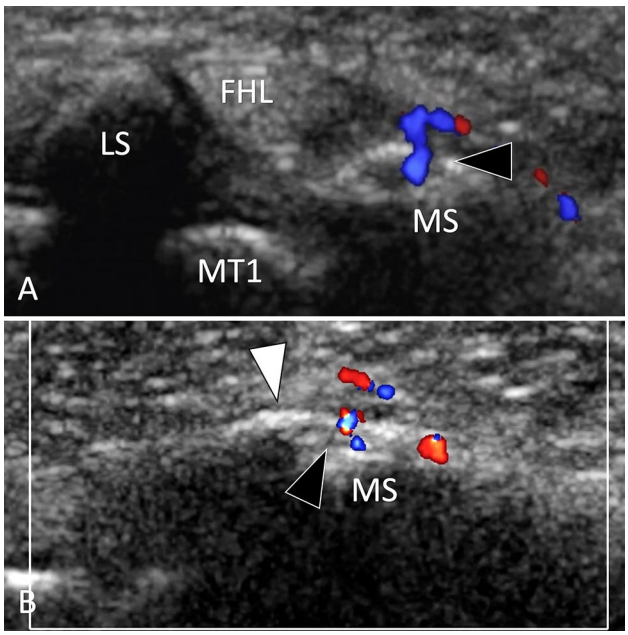

Fig. 35 Stress fracture. MTP sesamoids. **a**, **b** Axial (**a**) and sagittal (**b**) colour Doppler sonograms. US shows a focal break (black arrowhead) of the medial sesamoid (MS) associated with periosteal thickening (white arrowheads) and hyperaemia. The lateral sesamoid (LS) is normal. *MT1* first metatarsal, *FHKL* flexor hallucis longus tendon

a cartilaginous cap. Since OCs alter the contour of the bone surfaces, they can be detected by US [113]. The diagnosis of OCs is mostly made because of their pathognomonic appearance on radiographs. Nevertheless, asymptomatic OCs can be detected fortuitously by US. US has two potentials in the assessment of OC. First, it can accurately judge the thickness of the cartilaginous cap (Fig. 37) which is related to an eventual chondrosarcoma transformation, and second, it can judge local soft-tissue complications such as bursitis (Fig. 38).

US has very limited capabilities in assessing other bone tumours. The only possibility is when the outer cortex is interrupted by the tumour. In these cases, US can, through the "cortical window", detect an intra-osseous mass [2, 114] and assess the extent of the tumour in soft tissues (Fig. 39).

In tumours of the soft tissues adjacent to the bone cortex, pressure erosions (scalloping) on the local cortex can be detected by US and facilitate the detection of tumours (Fig. 40).

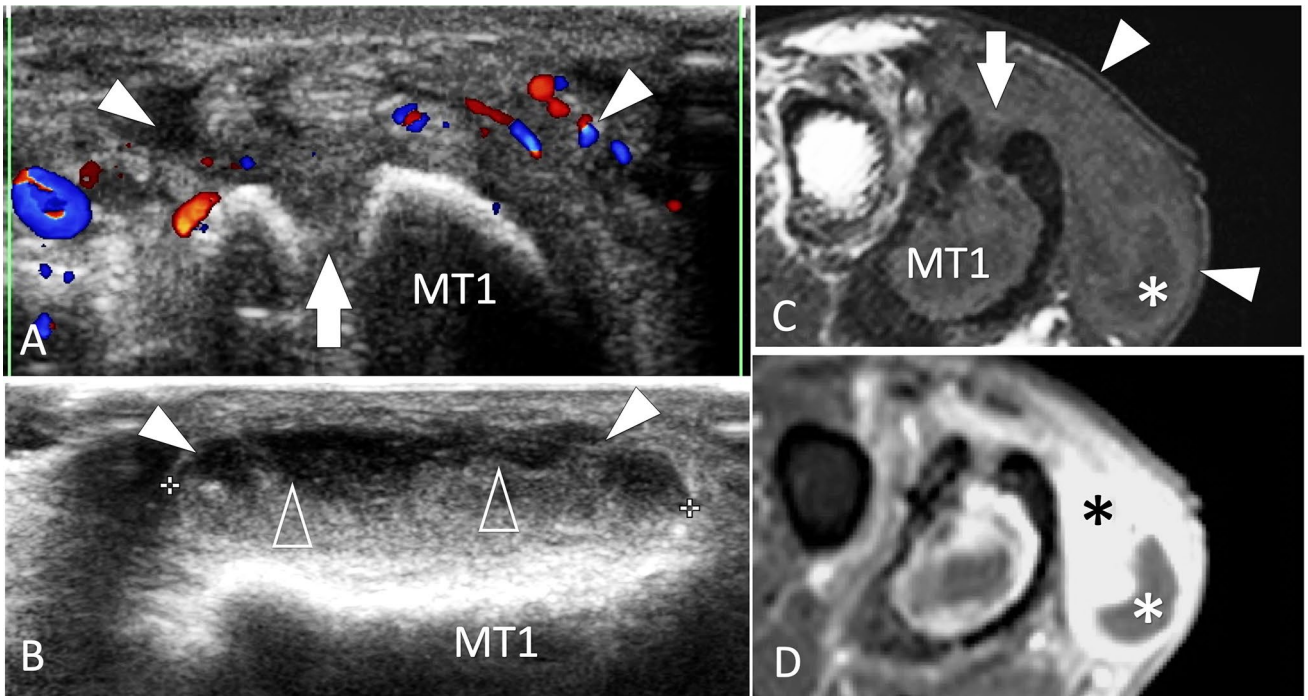

Fig. 36 Infection. Metatarsal. **a**, **b** Axial colour Doppler (**a**) and sagittal conventional (**b**) sonograms. **c**, **d** axial T1-weighted MR images obtained before (**c**) and after (**d**) i.v. contrast administration. US shows a focal break (white arrow) of the superior cortex of the first metatarsal (MT1) related to the previous surgery for chronic osteomyelitis. An abscess (white arrowheads) of the adjacent soft tissues appears on US as an irregular area with peripheral hyperaemia and a fluid–fluid level (void arrowheads). MRI confirms the US appearance. A small fluid collection is located at the plantar aspect of the abscess (white asterisk) surrounded by an area of contrast enhancement (black asterisk)

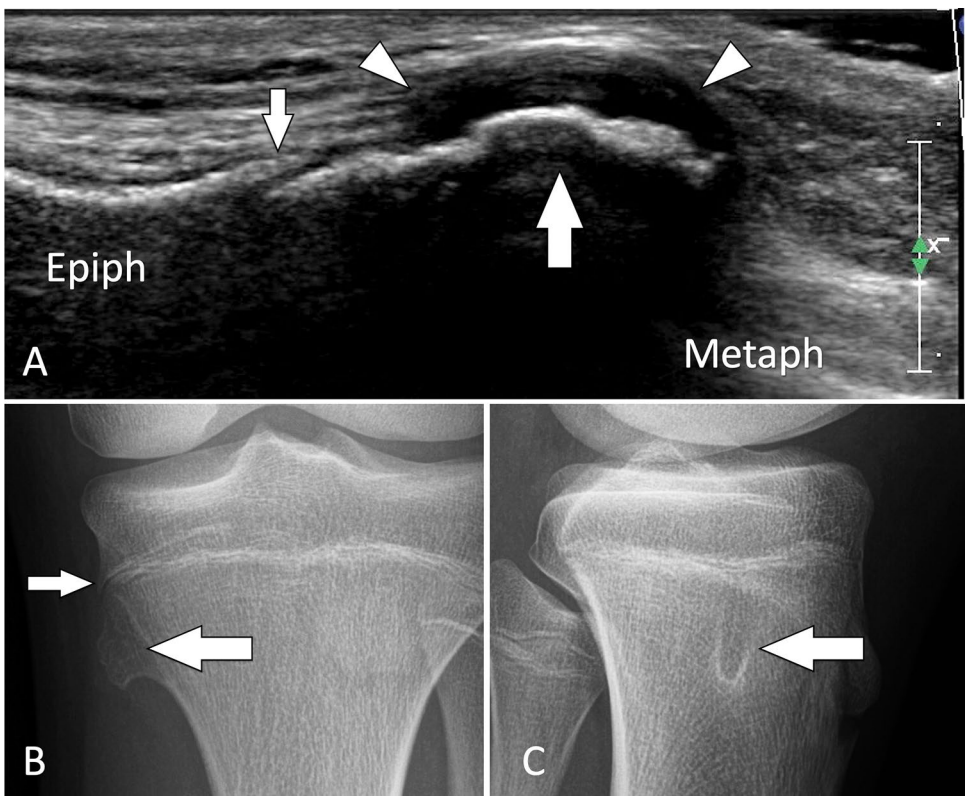

Fig. 37 Tumour. Solitary osteochondroma in an asymptomatic paediatric patient. **a** Coronal conventional sonogram obtained over the medial aspect of the proximal tibia in a paediatric patient with a suspicion of pes anserinus tendinitis. **b**, **c** A-P (**b**) and L-L (**c**) standard radiographs obtained after US. US discloses a focal bulging (large white arrow) of the cortical bone contour just distal to the growing cartilage of the proximal tibia (small white arrow). Note regular thick cartilage cap (white arrowheads). The US appearance is that of an osteochondroma. Standard radiographs confirm the US findings

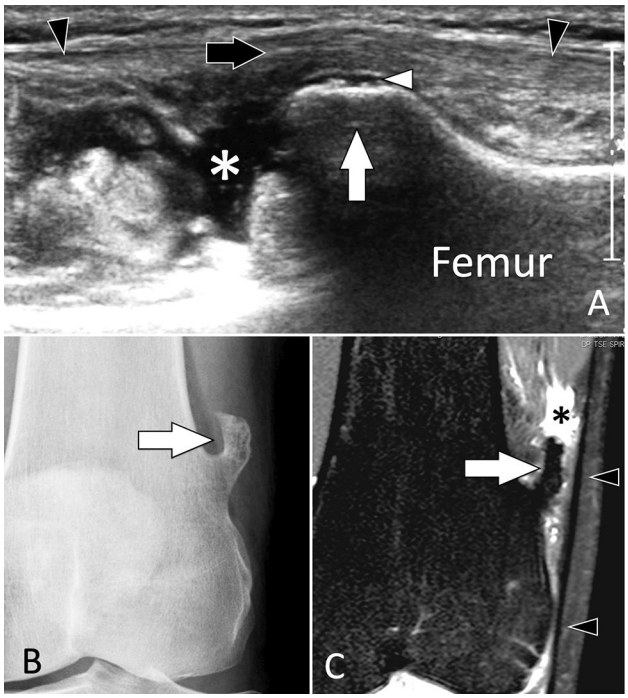

Fig. 38 Tumour. Solitary osteochondroma in a symptomatic adult. **a** Coronal conventional sonogram obtained over the lateral aspect of the distal femur in an adult with suspicion of iliotibial band syndrome. **b** A-P radiograph and coronal STIR MR image (**c**) obtained after US. US discloses an osteochondroma (large white arrow) covered by a thin cartilage cap (white arrowhead). The osteochondroma displaces the iliotibial band (black arrowheads) which appears hypoechoic and slightly irregular. As a result of local frictions during knee movements, a bursitis is detected by US as a fluid collection (asterisk) located proximally to the osteochondroma. The US appearance is that of an osteochondroma. Standard radiographs show the osteochondroma. MRI confirms the bursitis (asterisk) secondary to frictions of the iliotibial band (black arrowheads) against the osteochondroma

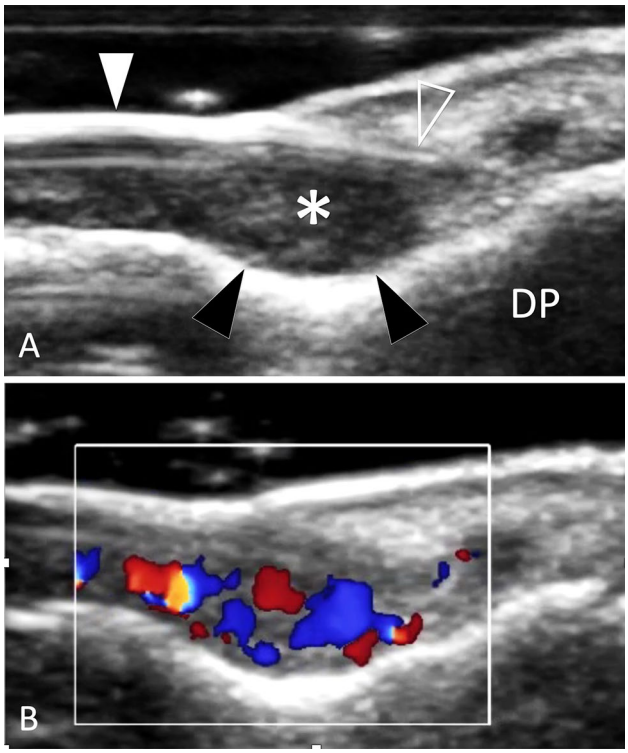

Fig. 40 Tumour. Glomus tumour. **a**, **b** Sagittal conventional (**a**) and colour Doppler (**b**) sonograms obtained over distal phalanx (DP) of the third finger. The glomus tumour (asterisk) presents as an ill-defined ovular mass located between the nail (white arrowhead) matrix (void arrowhead) and the superficial bone cortex. Note scalloping of the cortex (black arrowheads) due to chronic local pressure. In **b,** the tumour shows internal vascular signals

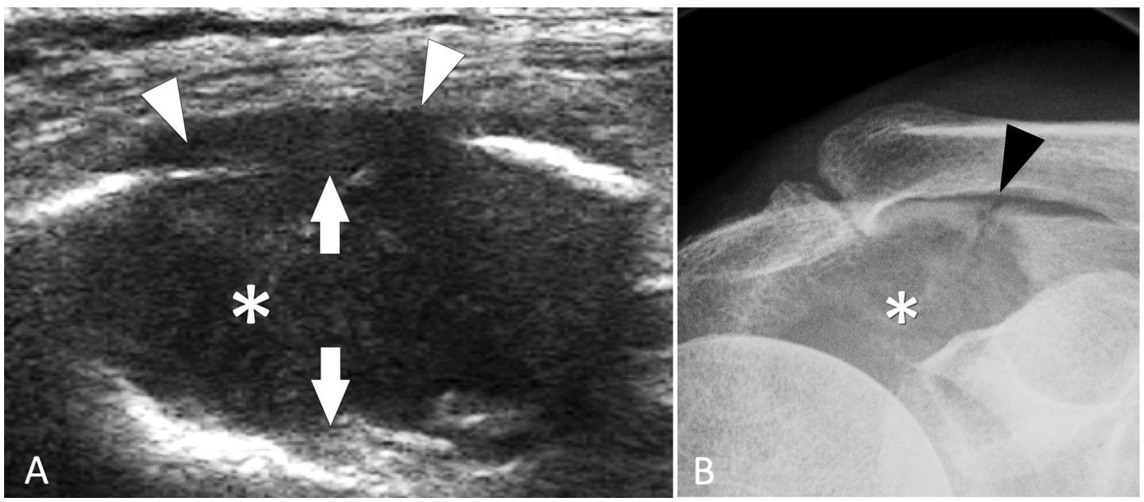

Fig. 39 Tumour. Metastasis. **a** Coronal conventional sonogram obtained over the spine of the scapula in a patient with night shoulder pain. **b** A-P standard radiographs obtained after US. US discloses a hypoechoic mass (asterisk) located inside the spine of the scapula. The mass is associated to osteolysis (white arrows) of the superficial and deep cortex. Note extension of the mass into the soft tissues (white arrowheads). **b** Standard radiograph shows an osteolytic lesion (asterisk) associated with a pathologic fracture (black arrowhead)

Compliance with ethical standards

Conflict of interest All authors has nothing to disclose.

Ethical standards statement All human studies have been approved by the appropriate ethics committee and have, therefore, been performed in accordance with the ethical standards laid down in the Helsinki Declaration of 1975 and its late amendments.

Informed consent None.

References

1. Zamorani MP, Valle M (2007) Bone and joint. In: Bianchi S, Martinoli C (eds) Ultrasound of the musculoskeletal system. Springer, Berlin, Heidelberg
2. Cho KH, Lee YH, Lee SM, Shahid MU, Suh KJ, Choi JH (2004) Sonography of bone and bone-related diseases of the extremities. J Clin Ultrasound. 32(9):511–521
3. Mariano J, Juana L, Iturbide I et al (2016) Rol de la ecografía en la evaluación de la cortical ósea. Rev Argent Radiol. https://doi.org/10.1016/j.rard.2015.11.002
4. Moraux A, Gitto S, Bianchi S (2019) Ultrasound features of the normal and pathologic periosteum. J Ultrasound Med 38:775–784
5. Morvan G, Brasseur J, Sans N (2005) Echographie de la surface du squelette [Superficial US of superficial bones]. J Radiol 86(12 Pt 2):1892–1903
6. Papalada A, Malliaropoulos N, Tsitas K, Kiritsi O, Padhiar N, Del Buono A, Maffulli N (2012) Ultrasound as a primary evaluation tool of bone stress injuries in elite track and field athletes. Am J Sports Med 40(4):915–919
7. Dwek JR (2010) The periosteum: what is it, where is it, and what mimics it in its absence? Skelet Radiol 39(4):319–323
8. Lawson JP (1994) International skeletal society lecture in honour of Howard D. Dorfman. Clinically significant radiologic anatomic variants of the skeleton. Am J Roentgenol 163:249–255
9. Mellado JM, Ramos A, Salvadó E, Camins A, Danús M, Saurí A (2003) Accessory ossicles and sesamoid bones of the ankle and foot: imaging findings, clinical significance and differential diagnosis. Eur Radiol 13(Suppl 6):L164–L177
10. Lawson JP (1990) Not-so-normal variants. Orthop Clin North Am 21:483–495
11. McMahon SE, LeRoux JA, Smith TO (2016) Hing CB The management of the painful bipartite patella: a systematic review. Knee Surg Sports Traumatol Arthrosc 24(9):2798–2805
12. Johnston PS, Paxton ES, Gordon V, Kraeutler MJ, Abboud JA, Williams GR (2013) Os acromiale: a review and an introduction of a new surgical technique for management. Orthop Clin North Am 44(4):635–644
13. Ouellette H, Thomas BJ, Kassarjian A et al (2007) Re-examining the association of os acromiale with supraspinatus and infraspinatus tears. Skelet Radiol 36:835–839
14. Horton S, Smuda MP, Jauregui JJ, Nadarajah V, Gilotra MN, Henn RF 3rd, Hasan SA (2019) Management of symptomatic os acromiale: a survey of the American shoulder and elbow surgeons. Int Orthop. https://doi.org/10.1007/s00264-018-4269-0**(Epub ahead of print; PubMed PMID: 30607498)**
15. Saupe E (1943) Primäre knochenmarkseiterung der kniescheibe. Deutsche Z Chir 258:386–392
16. Blankstein A, Cohen I, Salai M, Diamant L, Chechick A, Ganel A (2001) Ultrasonography: an imaging modality enabling the diagnosis of bipartite patella. Knee Surg Sports Traumatol Arthrosc 9(4):221–224
17. Tuthill HL, Finkelstein ER, Sanchez AM, Clifford PD, Subhawong TK, Jose J (2014) Imaging of tarsal navicular disorders: a pictorial review. Foot Ankle Spec 7(3):211–225
18. Davis DL (2017) Hook of the hamate: The spectrum of often missed pathologic findings. AJR Am J Roentgenol 209(5):1110–1118
19. Bianchi S, Hoffman D (2013) Ultrasound of talocalcaneal coalition: retrospective study of 11 patients. Skelet Radiol 42:1209–1214
20. Alaia EF, Rosenberg ZS, Bencardino JT, Ciavarra GA, Rossi I, Petchprapa CN (2016) Tarsal tunnel disease and talocalcaneal coalition: MRI features. Skelet Radiol 45(11):1507–1514
21. Hyer CF, Dawson JM, Philbin TM, Berlet GC, Lee TH (2005) The peroneal tubercle: description, classification, and relevance to peroneus longus tendon pathology. Foot Ankle Int 26(11):947–950
22. Saupe N, Mengiardi B, Pfirrmann CW, Vienne P, Seifert B, Zanetti M (2007) Anatomic variants associated with peroneal tendon disorders: MR imaging findings in volunteers with asymptomatic ankles. Radiology 242(2):509–517
23. Bruce WD, Christofersen MR, Phillips DL (1999) Stenosing tenosynovitis and impingement of the peroneal tendons associated with hypertrophy of the peroneal tubercle. Foot Ankle Int 20(7):464–467
24. Molini L, Bianchi S (2014) US in peroneal tendon tear. J Ultrasound 17:125–134
25. Bianchi S, Delmi M, Molini L (2010) Ultrasound of peroneal tendons. Semin Musculoskelet Radiol 14:292–306
26. Huang JI, Thayer MK, Paczas M, Lacey SH, Cooperman DR (2018) Variations in hook of hamate morphology: a cadaveric analysis. J Hand Surg Am. https://doi.org/10.1016/j.jhsa.2018.08.007
27. Chow JC, Weiss MA, Gu Y (2005) Anatomic variations of the hook of hamate and the relationship to carpal tunnel syndrome. J Hand Surg Am 30(6):1242–1247
28. Celi J, de Gautard G, Della Santa JD, Bianchi S (2008) Sonographic diagnosis of a radiographically undiagnosed hook of the hamate fracture. J Ultrasound Med 27(8):1235–1239
29. Itsubo T, Uchiyama S, Takahara K, Nakagawa H, Kamimura M, Miyasaka T (2004) Snapping wrist after surgery for carpal tunnel syndrome and trigger digit: a case report. J Hand Surg Am 29(3):384–386
30. Wirth MA, Lyons FR, Rockwood CA Jr (1993) Hypoplasia of the glenoid. A review of sixteen patients. J Bone Jt Surg Am. 75(8):1175–1184
31. Choi PJ, Iwanaga J, Tubbs RS (2017) A comprehensive review of the sternal foramina and its clinical significance. Cureus. 9(12):e1929 **(Published 2017 Dec 8)**
32. Bhootra BL (2004) Fatality following a sternal bone marrow aspiration procedure: a case report. Med Sci Law 44:170–172
33. Babinski MA, de Lemos L, Babinski MS, Gonçalves MV, De Paula RC, Fernandes RM (2015) Frequency of sternal foramen evaluated by MDCT: a minor variation of great relevance. Surg Radiol Anat 37(3):287–291
34. Nickson C, Rippey J (2011) Ultrasonography of sternal fractures. Australas J Ultrasound Med 14(4):6–11
35. Rutten MJ, Collins JM, de Waal Malefijt MC, Kiemeney LA, Jager GJ (2010) Unsuspected sonographic findings in patients with post-traumatic shoulder complaints. J Clin Ultrasound. 38(9):457–465
36. Copercini M, Bonvin F, Bianchi S et al (2003) Sonographic diagnosis of talar lateral process fracture. J Ultrasound Med 22:635–640

37. Hoffman DF, Adams E, Bianchi S (2015) Ultrasonography of fractures in sports medicine. Br J Sports Med 49(3):152–160
38. Nicholson JA, Tsang STJ, MacGillivray TJ, Perks F, Simpson AHRW (2019) What is the role of ultrasound in fracture management? Diagnosis and therapeutic potential for fractures, delayed unions, and fracture-related infection. Bone Jt Res 8(7):304–312
39. Craig JG, Jacobson JA, Moed BR (1999) Ultrasound of fracture and bone healing. Radiol Clin North Am 37(4):737–751
40. Ortiguera CJ, Buss DD (2002) Surgical management of the symptomatic os acromiale. J Shoulder Elbow Surg. 11(5):521–528
41. McCrady BM, Schaefer MP (2011) Sonographic visualisation of a scapular body fracture: a case report. J Clin Ultrasound 39(8):466–468
42. Botchu R, Lee KJ, Bianchi S (2012) Radiographically undetected coracoid fractures diagnosed by sonography. Report of seven cases. Skelet Radiol 41(6):693–698
43. Bianchi S, Jacob D, Lambert A, Draghi F (2017) Ultrasound of the coracoid process region: a pictorial essay. J Ultrasound Med 36(2):375–388
44. Patten RM, Mack LA, Wang KY, Lingel J (1992) Non-displaced fractures of the greater tuberosity of the humerus: sonographic detection. Radiology 182(1):201–204
45. Griffith JF, Rainer TH, Ching AS et al (1999) Sonography compared with radiography in revealing acute rib fracture. AJR Am J Roentgenol 173:1603–1609
46. Battistelli JM (1993) Anselem B [Echography in injuries of costal cartilages]. J Radiol 74:409–412
47. Turk F, Kurt AB, Saglam S (2010) Evaluation by ultrasound of traumatic rib fractures missed by radiography. Emerg Radiol 17(6):473–477
48. Malghem J, Vande Berg B, Lecouvet F et al (2001) Costal cartilage fractures as revealed on CT and sonography. AJR 176:429–432
49. Bortolotto C, Federici E, Draghi F, Bianchi S. Infraradiological displaced costal cartilage fracture in an athlete: ultrasound appearance. J Clinical Ultrasound in press
50. You JS, Chung YE, Kim D, Park S, Chung SP (2010) Role of sonography in the emergency room to diagnose sternal fractures. J Clin Ultrasound. 38(3):135–137
51. Pavić R, Margetić P, Hnatešen D (2015) Diagnosis of occult radial head and neck fracture in adults. Injury 46(Suppl 6):S119–S124
52. Carpenter CR, Pines JM, Schuur JD, Muir M, Calfee RP, Raja AS (2014) Adult scaphoid fracture. Acad Emerg Med 21(2):101–121
53. Platon A, Poletti PA, Van Aaken J, Fusetti C, Della Santa D, Beaulieu JY, Becker CD (2011) Occult fractures of the scaphoid: the role of ultrasonography in the emergency department. Skelet Radiol 40(7):869–875
54. Fusetti C, Poletti PA, Pradel PH et al (2005) Diagnosis of occult scaphoid fracture with high-spatial-resolution sonography: a prospective blind study. J Trauma 59:677–681
55. Hauger O, Bonnefoy O, Moinard M et al (2002) Occult fractures of the waist of the scaphoid: early diagnosis by high spatial resolution sonography. AJR Am J Roentgenol 178:1239–1245
56. Luong DH, Smith J, Bianchi S (2014) Flexor carpi radialis tendon ultrasound pictorial essay. Skelet Radiol 43(6):745–760
57. Kato H, Nakamura R, Horii E et al (2000) Diagnostic imaging for fracture of the hook of the hamate. Hand Surg 5(1):19–24
58. Pajares-López M, Hernández-Cortés P, Robles-Molina MJ (2011) Rupture of small finger flexor tendons secondary to asymptomatic non-union of the hamate hook. Orthopedics 34(2):142
59. Maier RM, Hughes M, Katranji A (2016) Patient with a hook of the hamate fracture presenting as vascular occlusion: diagnosis made with bedside ultrasound. J Emerg Med 51(1):63–65
60. Botchu R, Bianchi S (2014) Sonography of trapezial ridge fractures. J Clin Ultrasound 42(4):241–244
61. Van der Lei B, Van der Linden E, Mooyaart EL, Klasen HJ (1995) Fracture of the thumb sesamoid bone: a report of three cases and a review of the English-language literature. J Trauma Inj Infect Crit Care 38:836–840
62. Becciolini M, Bonacchi G (2015) Fracture of the sesamoid bones of the thumb associated with volar plate injury: ultrasound diagnosis. J Ultrasound 18:395–403
63. Bianchi S, Becciolini M (2019) Ultrasound evaluation of sesamoid fractures of the hand: retrospective report of 13 patients. J Ultrasound Med 38:1913–1920
64. Chun WJ, Checa A (2011) Patellar fracture masked by concomitant prepatellar bursitis: clinic-based ultrasonographic findings. J Clin Rheumatol 17(5):289
65. Pearce T, Cobby M (2011) Radiographically occult fracture of the tibial epiphysis: sonographic findings with CT correlation. J Clin Ultrasound 39(7):425–426
66. Kardouni JR (2012) Distal fibula fracture diagnosed with ultrasound imaging. J Orthop Sports Phys Ther 42(10):887
67. Wang CL, Shieh JY, Wang TG, Hsieh FJ (1999) Sonographic detection of occult fractures in the foot and ankle. J Clin Ultrasound 27:421–425
68. Boutry N, Vanderhofstadt A, Peetrons P (2006) Ultrasonography of anterosuperior calcaneal process fracture report of 2 cases. J Ultrasound Med. 25:381–385
69. Sabour S (2014) Bedside ultrasonography as a diagnostic tool for the fifth metatarsal fractures: methodological concern in reliability analysis. Am J Emerg Med 32(5):470
70. Yesilaras M, Aksay E, Atilla OD, Sever M, Kalenderer O (2014) The accuracy of bedside ultrasonography as a diagnostic tool for the fifth metatarsal fractures. Am J Emerg Med 32(2):171–174
71. Young JW, Kostrubiak IS, Resnik CS, Paley D (1990) Sonographic evaluation of bone production at the distraction site in Ilizarov limb-lengthening procedures. AJR Am J Roentgenol 154:125–128
72. Maffulli N, Thornton A (1995) Ultrasonographic appearance of external callus in long bone fractures. Injury 26:5–12
73. Rosenauer R, Pezzei C, Quadlbauer S et al (2020) Complications after operatively treated distal radius fractures [published online ahead of print, 2020 Mar 19]. Arch Orthop Trauma Surg. https://doi.org/10.1007/s00402-020-03372-z
74. Erra C, Granata G, Liotta G et al (2013) Ultrasound diagnosis of bony nerve entrapment: case series and literature review. Muscle Nerve 48(3):445–450
75. Bodner G, Buchberger W, Schocke M, Bale R, Huber B, Harpf C et al (2001) Radial nerve palsy associated with humeral shaft fracture: evaluation with US—initial experience. Radiology 219:811–816
76. Bianchi S, van Aaken J, Glauser T, Martinoli C, Beaulieu JY, Della SD (2008) Screw impingement on the extensor tendons in distal radius fractures treated by volar plating: sonographic appearance. AJR Am J Roentgenol 191(5):W199–203
77. Guillin R, Botchu R, Bianchi S (2012) Sonography of orthopedic hardware impingement of the extremities. J Ultrasound Med 31(9):1457–1463
78. Bianchi S, Abdelwahab IF, Zwass A et al (1995) Sonographic evaluation of lipohaemarthrosis: clinical and in vitro study. J Ultrasound Med 14:279–282
79. Aponte EM, Novik JI (2013) Identification of lipohaemarthrosis with point-of-care emergency ultrasonography: case report and brief literature review. J Emerg Med 44(2):453–456
80. Yabe M, Suzuki M, Hiraoka N et al (2000) A case of intra-articular fracture of the knee joint with three layers within lipohaemarthrosis by ultrasonography and computed tomography. Radiat Med 18:319

81. Khoury V, Van Lancker HP, Martineau PA (2013) Sonography as a tool for identifying engaging Hill–Sachs lesions: preliminary experience. J Ultrasound Med 32(9):1653–1657
82. Bianchi S, Martinoli C (1999) Detection of loose bodies in joints. Radiol Clin North Am 37(4):679–690
83. Tuijthof GJ, Kok AC, Terra MP, Aaftink JF, Streekstra GJ, van Dijk CN, Kerkhoffs GM (2013) Sensitivity and specificity of ultrasound in detecting (osteo)chondral defects: a cadaveric study. Ultrasound Med Biol 39(8):1368–1375
84. de Gautard G, de Gautard R, Bianchi S et al (2009) Sonography of jersey finger. J Ultrasound Med 28(3):389–392
85. Becciolini M, Bonacchi G, Bianchi S (2019) Ultrasound features of the proximal hamstring muscle-tendon-bone unit. J Ultrasound Med 38:1367–1382
86. Pesquer L, Poussange N, Sonnery-Cottet B et al (2016) Imaging of rectus femoris proximal tendinopathies. Skelet Radiol 45(7):889–897
87. Bianchi S, Bortolotto C, Draghi F (2017) Os peroneum imaging: normal appearance and pathological findings. Insights Imaging 8:59–68
88. Bianchi S, Gandolfo N, Witkowska-Luczach A (2011) Imagerie de l'os peroneum. In: Morvan G, Bianchi S, Bouysset M (eds) Le pied-Monographie de la SIMS, OPUS XXXVII. Saurapams, Montpellier, pp 319–239
89. Bousson V, Wybier M, Petrover D et al (2011) Les fractures de contrainte. J Radiol 92:188–207
90. Moran DS, Evans RK, Hadad E (2008) Imaging of lower extremity stress fracture injuries. Sports Med 38:345–356
91. Berger FH, de Jonge MC, Maas M (2007) Stress fractures in the lower extremity. The importance of increasing awareness amongst radiologists. Eur J Radiol 62(1):16
92. Matheson GO, Clement DB, Mckenzie DC, Taunton JE, Lloyd-Smith DR, Macintyre JG (1987) Stress fractures in athletes. Am J Sports Med 15:46–58
93. Behrens SB, Deren ME, Matson A, Fadale PD, Monchik KO (2013) Stress fractures of the pelvis and legs in athletes: a review. Sports health 5:165–174
94. Matcuk GR Jr, Mahanty SR, Skalski MR, Patel DB, White EA, Gottsegen CJ (2016) Stress fractures: pathophysiology, clinical presentation, imaging features, and treatment options. Emerg Radiol 23(4):365–375
95. Bianchi S, Jacob D (2018) Echography of stress fractures Échographie des fractures de stress. J de Traumatol du Sport 35:218–230
96. Khy V, Wyssa B, Bianchi S (2012) Bilateral stress fracture of the tibia diagnosed by ultrasound. A case report. J Ultrasound 15:130–134
97. Amoako A, Abid A, Shadiack A, Monaco R (2017) Ultrasound-diagnosed tibia stres fracture: a case report. Clin Med Insights Arthritis Musculoskelet Disord 10(10):1179544117702866. https://doi.org/10.1177/1179544117702866
98. Jones SL, Phillips M (2010) Early identification of foot and lower limb stress fractures using diagnostic ultrasonography: a review of three cases. Foot Ankle Online J 3:3
99. Bianchi S, Luong DH (2014) Stress fractures of the ankle malleoli diagnosed by ultrasound: a report of 6 cases. Skelet Radiol 43(6):813–818
100. Arni D, Lambert V, Delmi M, Bianchi S (2009) Insufficiency fracture of the calcaneum: sonographic findings. J Clin Ultrasound 37(7):424–427
101. Bianchi S, Luong DH (2018) Stress fractures of the calcaneus diagnosed by sonography: report of 8 cases. J Ultrasound Med 37(2):521–529
102. Mandell JC, Khurana B, Smith SE (2017) Stress fractures of the foot and ankle, part 2: site-specific etiology, imaging, and treatment, and differential diagnosis. Skelet Radiol 46(9):1165–1186
103. Sofka CM, Adler RS, Saboeiro GR, Pavlov H (2010) Sonographic evaluation and sonographic-guided therapeutic options of lateral ankle pain: peroneal tendon pathology associated with the presence of an os peroneum. HSS J 6:177–181
104. Royer M, Thomas T, Cesini J, Legrand E (2012) Stress fractures in 2011: practical approach. Joint Bone Spine Revue du Rhumatisme 79(Suppl 2):S86–90
105. Banal F, Gandjbakhch F, Foltz V, Goldcher A, Etchepare F, Rozenberg S, Koeger AC, Bourgeois P, Fautrel B (2009) Sensitivity and specificity of ultrasonography in early diagnosis of metatarsal bone stress fractures: a pilot study of 37 patients. J Rheumatol 36(8):1715–1719
106. Howard CB, Lieberman N, Mozes G, Nyska M (1992) Stress fracture detected sonographically. AJR Am J Roentgenol 159:1350–1351
107. Leininger AP, Fields KB (2010) Ultrasonography in early diagnosis of metatarsal bone stress fractures. Sensitivity and specificity. J Rheumatol 37(7):1543
108. Drakonaki EE, Garbi A (2010) Metatarsal stress fracture diagnosed with high-resolution sonography. J Ultrasound Med 29(3):473–476
109. Bodner G, Stockl B, Fierlinger A, Schocke M, Bernathova M (2005) Sonographic findings in stress fractures of the lower limb: preliminary findings. Eur Radiol 15:356–359
110. Chuckpaiwong B, Cook C, Pietrobon R, Nunley JA (2007) Second metatarsal stress fracture in sport: comparative risk factors between proximal and non-proximal locations. Br J Sports Med 41:510–514
111. Mandell JC, Khurana B (2017) Smith SE Stress fractures of the foot and ankle, part 1: biomechanics of bone and principles of imaging and treatment. Skelet Radiol 46:1021–1029
112. Balanika AP, Papakonstantinou O, Kontopoulou CJ et al (2009) Gray-scale and colour Doppler ultrasonographic evaluation of reactivated post-traumatic/postoperative chronic osteomyelitis. Skelet Radiol 38(4):363–369
113. Murphey MD, Choi JJ, Kransdorf MJ, Flemming DJ, Gannon FH (2000) Imaging of osteochondroma: variants and complications with radiologic-pathologic correlation. Radiographics 20(5):1407–1434
114. Malghem J, Vande Berg B, Noel H et al (1992) Benign osteochondromas and exostotic chondrosarcomas: evaluation of cartilage cap thickness by ultrasound. Skelet Radiol 21:33